Author Manuscript

Author Manuscript

Author Manuscript

Author Manuscript

HHS Public Access

Author manuscript

Cell Rep. Author manuscript; available in PMC 2022 February 08.

Published in final edited form as:

Cell Rep. 2021 December 21; 37(12): 110142. doi:10.1016/j.celrep.2021.110142.

Stepwise disassembly of GABAergic synapses during pathogenic excitotoxicity

Joshua D. Garcia[1], **Sara E. Gookin**[1], **Kevin C. Crosby**[1], **Samantha L. Schwartz**[1], **Erika Tiemeier**[2], **Matthew J. Kennedy**[1], **Mark L. Dell'Acqua**[1], **Paco S. Herson**[1,2], **Nidia Quillinan**[2], **Katharine R. Smith**[1,3,*]

[1]Department of Pharmacology, University of Colorado School of Medicine, Anschutz Medical Campus, 12800 East 19th Avenue, Aurora, CO 80045, USA

[2]Department of Anesthesiology, Neuronal Injury Program, University of Colorado School of Medicine, Anschutz Medical Campus, 12801 East 17th Avenue, Aurora, CO 80045, USA

[3]Lead contact

SUMMARY

GABAergic synaptic inhibition controls neuronal firing, excitability, and synaptic plasticity to regulate neuronal circuits. Following an acute excitotoxic insult, inhibitory synapses are eliminated, reducing synaptic inhibition, elevating circuit excitability, and contributing to the pathophysiology of brain injuries. However, mechanisms that drive inhibitory synapse disassembly and elimination are undefined. We find that inhibitory synapses are disassembled in a sequential manner following excitotoxicity: $GABA_AR$s undergo rapid nanoscale rearrangement and are dispersed from the synapse along with presynaptic active zone components, followed by the gradual removal of the gephyrin scaffold, prior to complete elimination of the presynaptic terminal. $GABA_AR$ nanoscale reorganization and synaptic declustering depends on calcineurin signaling, whereas disassembly of gephyrin relies on calpain activation, and blockade of both enzymes preserves inhibitory synapses after excitotoxic insult. Thus, inhibitory synapse disassembly occurs rapidly, with nanoscale precision, in a stepwise manner and most likely represents a critical step in the progression of hyperexcitability following excitotoxicity.

In brief

Elimination of inhibitory synapses following excitotoxic insult reduces synaptic inhibition and elevates neuronal excitability. Garcia et al. reveal that excitotoxicity-induced inhibitory synapse disassembly occurs sequentially, in a stepwise manner, and involves alterations to $GABA_AR$ and

This is an open access article under the CC BY-NC-ND license. http://creativecommons.org/licenses/by-nc-nd/4.0/

*Correspondence: katharine.r.smith@cuanschutz.edu.

AUTHOR CONTRIBUTIONS

Conceptualization, K.R.S. and J.D.G.; formal analysis and investigation, J.D.G., K.C.C., S.E.G., S.L.S., E.T., and K.R.S.; methodology, S.L.S. and K.C.C.; writing – original draft, J.D.G. and K.R.S.; writing – review & editing, J.D.G., K.R.S., K.C.C., and M.L.D.; supervision, K.R.S., M.L.D., M.J.K., N.Q., and P.H.; funding acquisition, K.R.S., J.D.G., M.L.D., M.J.K., N.Q., and P.H.

DECLARATION OF INTERESTS

The authors declare no competing interests.

SUPPLEMENTAL INFORMATION

Supplemental information can be found online at https://doi.org/10.1016/j.celrep.2021.110142.

Author Manuscript Author Manuscript Author Manuscript Author Manuscript

gephyrin nanoscale synaptic architecture, which is driven by independent calcineurin and calpain signaling pathways.

Graphical Abstract

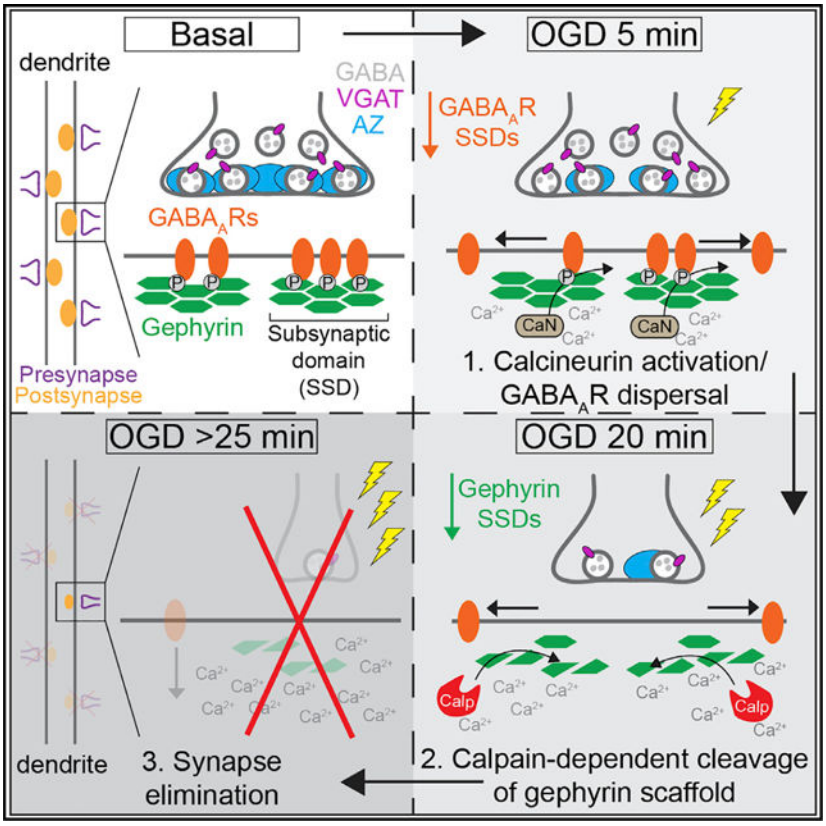

INTRODUCTION

The correct balance between excitation and inhibition in neuronal circuits is essential for learning, memory, cognition, and behavior (Klausberger and Somogyi, 2008; Smith and Kittler, 2010), and its disruption underlies the pathology of numerous brain disorders (Fritschy, 2008; Gao and Penzes, 2015). Synaptic inhibition in the brain is mediated by GABAergic inhibitory synapses, which regulate neuronal firing, neuron and circuit excitability, and synaptic plasticity (Chiu et al., 2019). The number of $GABA_A$ receptors ($GABA_A$Rs) clustered at inhibitory postsynaptic sites is a critical regulator of synaptic strength (Nusser et al., 1997), and rapid changes in synaptic receptor clustering drives GABAergic postsynaptic plasticity (Barberis, 2020; Oh and Smith, 2019). $GABA_A$Rs are clustered at synaptic sites by the principal inhibitory scaffolding protein, gephyrin (Tyagarajan and Fritschy, 2014), which cooperates with numerous other GABAergic synaptic proteins to organize and stabilize the synapse (Lorenz-Guertin and Jacob, 2018). $GABA_A$R synaptic abundance is tightly regulated by receptor trafficking to and from synaptic sites via lateral movement in the plasma membrane (Bannai et al., 2009; Battaglia et al., 2018; Muir et al., 2010), endocytosis (Kittler et al., 2005; Smith et al., 2008,

Author Manuscript Author Manuscript Author Manuscript Author Manuscript

2012), and recycling (Twelvetrees et al., 2010). However, these trafficking mechanisms are disrupted in numerous pathological situations, leading to increased excitability and neuron and circuit dysfunction (Mele et al., 2019; Smith and Kittler, 2010).

Changes in neuronal activity impact $GABA_AR$ trafficking by increasing or decreasing postsynaptic receptor clustering and thereby altering synaptic inhibition (Bannai et al., 2009, 2015; Battaglia et al., 2018; Muir et al., 2010; Petrini et al., 2014). Under physiological conditions, NMDA receptor (NMDAR) activation leads to $GABA_AR$ removal from the synapse, due to increased lateral diffusion of receptors on the plasma membrane, resulting in synaptic depression of GABAergic inputs (Bannai et al., 2009; Muir et al., 2010). In this situation, $GABA_AR$ loss from the synapse is reversible, making this depression transient and leaving the inhibitory synapse intact. In comparison, acute excitotoxic insults lead to complete elimination of inhibitory synapses and synaptic inhibition, a process that contributes to the pathophysiology of acute brain disorders, such as ischemia and epilepsy (El-Hassar et al., 2007; Mele et al., 2019). This loss of inhibitory synaptic drive drastically alters the balance between excitation and inhibition, induces circuit hyperexcitability, and contributes to disease progression (El-Hassar et al., 2007; Mele et al., 2019). $GABA_AR$ clustering and trafficking is acutely altered following excitotoxic insult, manifesting in increased receptor endocytosis (Blair et al., 2004; Goodkin et al., 2005; Mele et al., 2014; Naylor et al., 2005; Smith et al., 2012). Moreover, inhibitory synapses are lost, and synaptic inhibition is severely impaired in vulnerable brain regions in numerous animal models of ischemia and epilepsy (Goodkin et al., 2005; Mele et al., 2014, 2019; Naylor et al., 2005; Zhan et al., 2006). However, due to most imaging and electrophysiological analyses being performed hours to days following the excitotoxic insult, the precise molecular processes that lead to inhibitory synapse loss and impaired synaptic inhibition remain unknown.

Here, we used *in vitro* and *in vivo* models of ischemia to delineate the events that lead to inhibitory synapse disassembly following an excitotoxic insult. Our results reveal independent molecular mechanisms drive synaptic nanoscale rearrangements and the sequential loss of $GABA_ARs$, presynaptic active zone components, and gephyrin, prior to complete elimination of the presynaptic terminal.

RESULTS

Ischemic insult induces rapid removal of $GABA_ARs$ and gephyrin from GABAergic synaptic sites

To investigate the precise mechanistic steps that lead to inhibitory synapse elimination driven by excitotoxicity, we used cultured hippocampal neurons exposed to oxygen and glucose deprivation (OGD), an established *in vitro* model of global ischemia (Arancibia-Cárcamo et al., 2009; Smith et al., 2012, 2017). To determine whether pre- or postsynaptic components are lost from the synapse immediately following 30 min of OGD, we immunostained surface $GABA_ARs$ (γ2 subunit), gephyrin, and vesicular GABA transporter (VGAT) to label inhibitory presynaptic terminals (Figure 1A). $GABA_AR$ and gephyrin cluster area and density were reduced in both somatic and dendritic neuronal compartments within the first 30 min of OGD compared to controls (Figure 1B). In comparison, we observed no alterations to VGAT clustering within the same time frame, suggesting

Author Manuscript Author Manuscript Author Manuscript Author Manuscript

that postsynaptic components are removed from the synapse prior to disassembly of the presynaptic terminal (Figure 1B). To verify this, we stained for additional inhibitory pre- and postsynaptic proteins following the same 30 min OGD treatment (Figures S1A–S1D). We observed similar reductions in cluster area and density for the postsynaptic adhesion molecule neuroligin-2 (NL2) and α1 and β3 $GABA_AR$ subunits, indicating that other postsynaptic proteins are also rapidly lost during OGD (Figures S1A–S1D). Furthermore, analysis of the inhibitory presynaptic marker glutamic acid decarboxylase (GAD67) revealed little change in clustering following OGD, mirroring our observations of VGAT clusters (Figures S1C and S1D). We also assessed whether the loss of $GABA_ARs$ and gephyrin was reversible by reperfusing neurons following 30 min of OGD treatment (Figure S1E). We observed no recovery of $GABA_ARs$ or gephyrin following 30 min or 2 h of reperfusion, and VGAT clustering was also decreased (Figures S1E and S1F). Thus, removal of these inhibitory synaptic proteins during OGD appears to be permanent.

To confirm inhibitory synapses are disassembled in a similar way *in vivo*, we analyzed GABAergic synapses in hippocampal tissue from mice that had undergone cardiac arrest and cardiopulmonary resuscitation (CA/CPR), a well-characterized model of global ischemia reperfusion injury (Buonarati et al., 2020). CA was induced by KCl injection; after 8 min, mice were resuscitated by epinephrine injection, mechanical ventilation, and chest compressions. Mice were monitored for 15 min prior to perfusion fixation, thereby providing the most acute insult possible, to mimic our *in vitro* paradigm. We immunostained hippocampal sections for synaptic $GABA_ARs$, gephyrin, and VGAT and imaged the CA1 *Stratum pyramidale* and *radiatum* regions (Figure 1C). Similar to our results in vitro, we observed decreased $GABA_AR$ and gephyrin cluster area and density in both regions from CA/CPR mice, compared with sham mice (Figure 1D). There were no changes in VGAT clustering in either region (Figure 1D). Together, these *in vitro* and *in vivo* data show that the onset of both OGD and CA/CPR induce rapid excitotoxic inhibitory synapse disassembly through the loss of inhibitory postsynaptic compartments, preceding alterations to the GABAergic presynaptic terminal.

$GABA_ARs$ are lost prior to gephyrin during excitotoxic-induced inhibitory synapse disassembly

We then asked when $GABA_ARs$ and gephyrin are removed from the synapse and whether this occurs simultaneously or at different time points throughout the 30-min OGD insult. To further quantify the loss of $GABA_ARs$ and gephyrin from synaptic sites, we used super-resolution, three-dimensional structured illumination microscopy (3D-SIM) (Figure 2A), which we have previously optimized for detailed imaging of GABAergic synapses (Crosby et al., 2019). 3D-SIM provides three-color imaging with enhanced resolution, thereby enabling precise measurements of $GABA_AR$ and gephyrin synaptic compartments as they shrink below the resolution limit of conventional confocal imaging. To determine when $GABA_ARs$ and gephyrin are removed from the synapse, hippocampal neurons were exposed to OGD conditions for increasing 5-min increments up to a maximum of 25 min. Neurons were then immunostained for surface $GABA_ARs$, gephyrin, and VGAT, and dendrites were imaged with 3D-SIM (Figure 2A). Synapses were selected for 3D segmentation analysis (see STAR Methods and Crosby et al., 2019), which computes the volume of $GABA_AR$

Author Manuscript Author Manuscript Author Manuscript Author Manuscript

or gephyrin immunofluorescence at VGAT-positive synapses, providing a "compartment volume" for each synaptic component (Crosby et al., 2019). We observed a rapid and robust reduction (~59.7%) in $GABA_AR$ compartment volume within 5 min of OGD onset, which was maintained at each time point up to 25 min (Figure 2B). In comparison, reduction of the gephyrin compartment volume was first detectable at 15 min following OGD onset, with the greatest reduction in volume (60.1%) at the 20- and 25-min time points (Figure 2B). To allay any concerns about gephyrin antibody specificity (Kuhse et al., 2012), we assessed gephyrin clustering with an alternative gephyrin antibody (Niwa et al., 2019; Figures S2A and S2B) and found a similar pattern of gephyrin cluster shrinkage following OGD. As NL2 was also lost from the synapse within 30 min of OGD onset (Figures S1A and S1B), we monitored its removal over the OGD time course and found it was lost from the synapse gradually and did not mirror either $GABA_AR$ or gephyrin removal (Figures S2C and S2D). In comparison with these postsynaptic proteins, the volume of the presynaptic VGAT compartment was unaltered throughout the first 20 min of the OGD insult and was only reduced after 25 min (Figure 2B), suggesting that loss of the inhibitory presynaptic terminal is delayed compared with that of $GABA_ARs$ and gephyrin.

We also examined the percentage of synapses with $GABA_ARs$ and gephyrin (identified by VGAT labeling). Under basal conditions, 97.5% of synapses contained $GABA_ARs$ and 100% contained gephyrin (Figure 2C). Following 5 min of OGD, there was an ~30% decrease in the percentage of synapses with $GABA_AR$ immunofluorescence (Figure 2C), indicating that, at many synapses, $GABA_ARs$ were completely removed by this time point. The percentage of synapses lacking $GABA_ARs$ increased steadily to a maximum of ~43% at 25 min following OGD onset (Figure 2C). The percentage of synapses without gephyrin was negligible at the 5- and 10-min time points but increased gradually over the 15-, 20-, and 25-min time points (Figure 2C). We also observed a slight reduction in VGAT density at 15 and 20 min following OGD onset, with a more profound ~48% reduction at 25 min (Figure 2C), indicating that, by these later time points, whole synapses will have likely been eliminated. This was in contrast with our confocal data that showed no changes in VGAT cluster area or density following OGD or CA/CPR, thus highlighting the greater accuracy of our 3D-SIM approach. To investigate whether specific synapse populations were lost during OGD, we analyzed the distribution of synaptic volumes (the total volume of $GABA_ARs$, gephyrin, and VGAT) in control and OGD conditions. We fitted the data to models that either assumed a single normal or mix of two normal distributions (see STAR Methods). Synapse volumes in control conditions fitted significantly better to a biphasic distribution (F-test: $p = 3.7 \times 10^{-5}$), which revealed 2 distinct synapse populations with mean volumes of 0.11 μm^3 and 0.22 μm^3 (mu1 and mu2; Figure S3A). Synapse volumes from the OGD data also fit better to the mix of two normal distributions (F-test: $p = 0.007$), although with smaller means for the two populations (mu1 = 0.05 μm^3; mu2 = 0.11 μm^3). Notably, the larger population of synapses observed in control conditions was completely absent in the OGD dataset, indicating their loss following OGD. The OGD data revealed a similar proportion of synapses had a mean volume of 0.11 μm^3, as in the control data, but a new population of smaller synapses also emerged (mu1 = 0.05 μm^3), indicating significant synapse shrinkage at this time point.

Author Manuscript Author Manuscript Author Manuscript Author Manuscript

Presynaptic active zone proteins are removed prior to complete disassembly of the presynaptic terminal

Our data indicate that removal of inhibitory axon terminals following OGD is delayed compared with postsynaptic proteins but provides no information on whether any form of sequential disassembly occurs presynaptically. To address this, we imaged bassoon and Rab3 interacting molecule (RIM1), key molecular components that localize to the active zone, the site of presynaptic neurotransmitter release, and the principal contact site between the pre- and postsynaptic specializations (Südhof, 2012). In contrast to the stability of VGAT-labeled presynaptic terminals, analysis of RIM and bassoon immunofluorescence at VGAT-positive synapses revealed an immediate reduction in compartment volumes at 5 min of OGD, which was maintained up to 25 min following OGD (Figures 2D–2F). This suggests that the active zone is disassembled rapidly following OGD onset and precedes the loss of the inhibitory presynaptic terminal.

Rapid nanoscale alterations to $GABA_AR$ sub-synaptic domains immediately following OGD induction

$GABA_A$Rs and gephyrin are organized into nanoscale sub-synaptic domains (SSDs) that have important roles in overall synapse function and plasticity (Crosby et al., 2019; Pennacchietti et al., 2017; Specht et al., 2013). We have shown that SSDs of $GABA_A$Rs and gephyrin emerge in GABAergic synapses as they grow during activity-dependent synaptic plasticity (Crosby et al., 2019). Yet few studies have shown how GABAergic synapses shrink and disassemble due to the technical challenges of imaging small synaptic structures. Because OGD reduces the total compartment volume of $GABA_A$Rs and gephyrin at GABAergic synapses, we hypothesized that nanoscale changes to the postsynaptic domain might accompany compartment shrinkage and $GABA_A$R and gephyrin removal from synapses. Figure 3A shows high-magnification 3D-SIM images of dendritic inhibitory synapses that have undergone OGD insult for increasing lengths of time. We used 3D segmentation analysis (Crosby et al., 2019) to quantify the volume and number of $GABA_A$R and gephyrin SSDs for each compartment at each time point (Figures 3B–3D). Within the first 5 min of OGD, the mean $GABA_A$R SSD volume was reduced by 56% compared to the control (Figure 3C). The mean number of $GABA_A$R SSDs per synapse was also reduced by ~31% during this same time frame (Figure 3D), indicating that $GABA_A$R SSDs likely shrink and are removed from the synapse. A reduction in the mean number of $GABA_A$R SSDs at 5 min is also reflected by a decrease in the percentage of synapses with multiple $GABA_A$R SSDs (multi) and the emergence of synapses with no $GABA_A$R SSDs (Figure S3B). By 5 min of OGD, the percentage of synapses with multi-SSDs decreased to ~16.4% and synapses without SSDs increased to ~27.5% (Figure S3B), indicating that an initial mechanistic step in synapse disassembly is nanoscale architectural rearrangement of $GABA_A$R SSDs. In contrast, there were negligible changes to gephyrin nanoscale distribution at the 5or 10-min time points (Figures 3C, 3D, and S3B). However, we observed gradual reductions in SSD volume and mean SSD numbers and a redistribution of synapses with either multi- or no SSDs for gephyrin at 15, 20, and 25 min following OGD insult (Figures 3C, 3D, and S3B), suggesting that similar nanoscale modifications lead to gephyrin shrinkage and removal from the synapse as with the $GABA_A$R.

Author Manuscript Author Manuscript Author Manuscript Author Manuscript

As OGD impacted GABAergic synapses in both dendritic and somatic neuronal compartments (Figure 1), we then assessed whether OGD-induced changes to $GABA_AR$ and gephyrin nanoscale organization at somatic synapses were similar to those at dendritic synapses. 3D-SIM of somatic inhibitory synapses following increasing lengths of OGD exposure revealed a gradual loss of $GABA_AR$ and gephyrin immunofluorescence from the synaptic site over time (Figure 3E). Analysis of somatic synapse volume distributions revealed a similar biphasic distribution (Figure S3C) and a similar loss of larger synapses following OGD, as shown for dendritic synapses (Figure S3A). Notably, $GABA_ARs$ and gephyrin were lost from the synapse in tandem (Figure 3F), rather than in a stepwise fashion as at dendritic synapses. Mean $GABA_AR$ SSD volume and number were also gradually reduced over time (Figures 3G, 3H, and S3D), compared with their rapid removal from dendritic synapses. Gephyrin nanoscale alterations also closely mirrored those of $GABA_ARs$ at somatic synapses (Figures 3G and 3H). These data support the existence of differential OGD-induced nanoscale rearrangements at dendritic and somatic inhibitory synapses, which likely underlie distinct synapse shrinkage mechanisms.

OGD induces rapid dispersal of $GABA_ARs$ from the gephyrin scaffold

Our 3D-SIM revealed that $GABA_AR$ nanoscale SSD volume and number are reduced immediately following OGD induction. $GABA_ARs$ move laterally in the plasma membrane, in and out of synapses to rapidly modulate synaptic strength (Petrini and Barberis, 2014). We therefore hypothesized that $GABA_AR$ SSD shrinkage and loss would be paralleled by a rapid decrease in receptor density in the gephyrin scaffold. To test whether OGD leads to rapid $GABA_AR$ dispersal, we performed direct stochastic optical reconstruction microscopy (dSTORM) (Heilemann et al., 2008; Rust et al., 2006) to map single-molecule localizations of $GABA_ARs$ relative to the gephyrin scaffold at VGAT-labeled synapses (Figures 4A and 4B). Figure 4A shows example dSTORM images of Alexa Fluor 647 surface-labeled $GABA_ARs$ and CF568-labeled gephyrin in neurons from control conditions or following a 5-min OGD insult. The area of the gephyrin scaffold was determined by using a density-based clustering algorithm on the gephyrin localizations (see STAR Methods). Figure 4B shows localization plots of $GABA_ARs$ relative to gephyrin in example synapses, the delineated gephyrin scaffold region, and the $GABA_AR$ localizations within or outside of the scaffold. Analysis of the gephyrin scaffold area and localization density confirmed no significant alterations to gephyrin following 5 min OGD (Figures 4C and 4D), which is in agreement with our 3D-SIM data. To test whether OGD induction rapidly reduced synaptic $GABA_AR$ abundance, we calculated the relative $GABA_AR$ enrichment within the gephyrin scaffold (a ratio between the scaffold $GABA_AR$ density and the overall $GABA_AR$ density within the surrounding area). Comparing this $GABA_AR$ density ratio in control conditions and following 5 min of OGD, we found that $GABA_AR$ enrichment within the gephyrin scaffold was robustly decreased following OGD, suggesting that $GABA_ARs$ rapidly disperse from gephyrin following the onset of OGD (Figure 4E).

Calcineurin activity is required for OGD-induced $GABA_AR$ nanoscale reorganization and removal from synapses

Under normal physiological conditions, the calcium-activated phosphatase, calcineurin (CaN) facilitates $GABA_AR$ dispersal from inhibitory synapses during synaptic depression

Author Manuscript Author Manuscript Author Manuscript Author Manuscript

(Bannai et al., 2009; Muir et al., 2010). Excitotoxicity also activates CaN during ischemic insult, where upstream NMDAR activation is required for CaN-dependent signaling. Thus, we hypothesized that CaN-dependent $GABA_AR$ loss from inhibitory synapses may be the first step in synapse disassembly during excitotoxicity. To investigate this possibility, we induced OGD for 30 min in the presence of the CaN inhibitors cyclosporin A (CsA) or FK506. We then labeled synaptic $GABA_ARs$, gephyrin, and VGAT; imaged hippocampal dendrites by confocal imaging; and performed cluster analysis (Figures 5A and 5B). This analysis revealed that blocking CaN activity with either inhibitor fully prevented OGD-induced reductions in $GABA_AR$ cluster area and density. Because a 30-min OGD insult promotes $GABA_AR$ endocytosis (Smith et al., 2012), we tested whether CaN activation is also required for OGD-induced reductions in surface $GABA_AR$ levels. We performed surface biotinylation of hippocampal cultures treated with OGD for 30 min, in the absence or presence of CaN inhibitors. We observed decreased surface $GABA_AR$ levels following 30 min of OGD compared to control conditions (Figure S4A), which was blocked by CsA and FK506 (Figure S4A), suggesting that CaN is also required for $GABA_AR$ internalization during excitotoxic synapse disassembly. In contrast to $GABA_AR$ removal by CaN, the inhibitors CsA and FK506 only partially prevented OGD-induced reductions in gephyrin cluster area and density, suggesting that other mechanisms may be responsible for gephyrin loss at postsynaptic sites (Figures 5A and 5B). Similar to CaN inhibition, blocking upstream NMDAR hyperactivity with APV prevented the declustering of $GABA_ARs$, as well as gephyrin shrinkage and removal (Figures S4B and S4C), as compared to partial retention with CaN inhibition alone. Thus, NMDAR hyperactivity and CaN activation are required for $GABA_AR$ removal from synapses, whereas gephyrin removal occurs through distinct mechanisms downstream of NMDAR activation.

Our 3D-SIM and dSTORM analyses show that $GABA_AR$ nanoscale architecture is altered within 5 min of OGD. Given that CaN activity is required for reduced $GABA_AR$ clustering during OGD, we next tested whether CaN activation is also required for rapid nanoscale alterations to synaptic $GABA_ARs$ (Figure 5C). We used 3D-SIM to determine compartment and SSD volume and SSD number in synapses) from hippocampal neurons treated with OGD for 5 min in the presence of CsA or control conditions (Figures 5C and 5D). As in Figure 3, $GABA_AR$ compartment volume, SSD volume, and SSD number were robustly decreased following the 5-min OGD insult compared to controls. However, this decrease was blocked upon CaN inhibition (Figure 5D), demonstrating that CaN is required for altered $GABA_AR$ nanoscale organization immediately following excitotoxic insult. We detected no changes to gephyrin SSD volume or number following the 5-min OGD insult with or without CsA, confirming that there were no nanoscale alterations to the gephyrin synaptic scaffold at this time point. In addition, dSTORM imaging of $GABA_ARs$ and gephyrin also showed that CaN inhibition prevented the declustering of $GABA_ARs$ from the gephyrin scaffold following 5 min of OGD (Figures 5E and 5F). As shown in Figure 4, exposure to OGD for 5 min induced rapid reduction in $GABA_AR$ enrichment in the gephyrin scaffold, which was strongly prevented by CsA application (Figures 5E and 5F).

$GABA_AR$ α1/2/3 and β2/3 subunits interact directly with gephyrin (Kowalczyk et al., 2013; Mukherjee et al., 2011; Tretter et al., 2008, 2011), thereby contributing to $GABA_AR$ synaptic stabilization. This led us to hypothesize that a reduction in the $GABA_AR$-gephyrin

Author Manuscript Author Manuscript Author Manuscript Author Manuscript

interaction might underlie the dispersal of $GABA_A$Rs from the synapse immediately following OGD onset. To test this hypothesis, we performed proximity ligation assays (PLAs) to assess the direct interaction between $GABA_A$R-α1 subunits and gephyrin following OGD (Figure S4D). In control conditions, we observed fluorescent PLA puncta throughout the dendrite, indicating the presence of the $GABA_A$R-gephyrin interaction (Figure S4D). Control experiments showed minimal PLA signal if either primary antibody was omitted or if neurons were non-permeabilized (given that the $GABA_A$R was N-terminally labeled; Figures S4E and S4F). Following 5 min of OGD, we observed an 75% decrease in the PLA puncta density, indicating a reduction in the $GABA_A$R-gephyrin association (Figure S4D). This decrease in PLA puncta density was blocked by CaN inhibition with CsA, suggesting that the loss of the $GABA_A$R-gephyrin interaction following OGD is CaN dependent (Figure S4D). Together, our super-resolution imaging and PLA data suggest that OGD-induced CaN activation is required for the rapid reorganization of $GABA_A$R nanoscale architecture and receptor removal from synaptic sites by decreasing the $GABA_A$R-gephyrin interaction, prior to any alterations to the gephyrin scaffold.

$GABA_A$R-γ2 serine 327 dephosphorylation controls OGD-dependent $GABA_A$R declustering

To determine how CaN controls $GABA_A$R synaptic declustering during OGD, we investigated the role of the key phospho-site, serine 327, on the γ2 $GABA_A$R subunit (γ2-S327), which is a regulator of $GABA_A$R clustering and inhibitory synaptic strength (Muir et al., 2010; Wang et al., 2003). We extracted whole-cell hippocampal lysates following 30 min of OGD or control conditions and performed western blot analysis to compare levels of phosphorylated γ2-S327 between conditions (Figure 6A). Quantification revealed an ~50% reduction in γ2-S327 phosphorylation levels following OGD, which was strongly blocked by CaN inhibition with both CsA and FK506 (Figure 6A). Similarly, hippocampal lysates from the CA/CPR mouse model also showed a reduction in γ2-S327 phosphorylation in CA/CPR samples compared to controls (Figure 6B). Given the reduction in γ2-S327 phosphorylation following both *in vitro* and *in vivo* excitotoxic insults, we then asked how fast γ2-S327 dephosphorylation occurred following OGD onset (Figure 6C) and whether γ2-S327 dephosphorylation kinetics aligned with CaN-mediated $GABA_A$R dispersal. We found that γ2-S327 was dephosphorylated rapidly, within the first 3 min of the insult, a similar time frame as CaN-dependent $GABA_A$R declustering and removal from synapses (Figures 2, 3, 4, and 6C).

To test whether γ2-S327 is involved in $GABA_A$R cluster loss following OGD, we expressed wild-type (WT) or phospho-null mutant (γ2-S327A) γ2-$GABA_A$Rs in hippocampal neurons and exposed them to control conditions or a 30-min OGD insult (Figure 6D). Figure S5 shows that expression of γ2-S327A did not alter $GABA_A$R cluster area or density under basal conditions compared to WT-expressing neurons or untransfected neighboring neurons within the same image. Following OGD, WT-$GABA_A$R clusters were reduced in area and density (Figure 6E), and similar reductions were observed in neighboring untransfected cells within the same image (Figure S5B). In comparison, γ2-S327A mutant $GABA_A$R cluster area and density were indistinguishable between control and OGD conditions, indicating that mutating S327 can prevent OGD-dependent $GABA_A$R declustering (Figures 6D and 6E). Importantly, neighboring untransfected neurons exhibited similar reductions

Author Manuscript Author Manuscript Author Manuscript Author Manuscript

in $GABA_AR$ cluster area and density as the WT-expressing neurons, suggesting that these effects are specifically due to the γ2-S327A mutation in transfected cells (Figure S5B). As with CaN inhibition (Figures 5A and 5B), $GABA_AR$ synaptic retention by the γ2-S327A mutant only partially prevented the loss of gephyrin from the synapse (Figure 6E), again indicating independent mechanisms drive gephyrin removal. Expression of either WT or mutant $GABA_AR$ had no effect on VGAT clustering (Figure 6E). Thus, γ2-S327 is an important regulator of $GABA_AR$ declustering during OGD insult.

OGD-induced gephyrin cleavage parallels removal of gephyrin from synaptic sites and underlies gephyrin nanoscale rearrangements

Given the limited effects of CaN inhibition in preventing OGD-induced gephyrin declustering, we reasoned that other signaling pathways might independently remove gephyrin from the synapse. The calcium-activated protease, calpain, has previously been demonstrated to target gephyrin under physiological conditions and in models of ischemia and epilepsy (Costa et al., 2016; González, 2019; Tyagarajan et al., 2011, 2013). However, no study has demonstrated a role for calpain in rapid inhibitory synapse disassembly, at the nanoscale level or immediately following excitotoxic insult. Calpain-dependent gephyrin cleavage results in 2 proteolytic products of ~45 and 100 kDa, which can be identified by western blot analysis of neuronal lysates (Figure 7A). To test whether gephyrin is rapidly cleaved within 30 min of OGD, we analyzed lysates from control and OGD-treated hippocampal neuronal cultures or hippocampal extracts from sham and CA/CPR-treated mice, using western blotting for the two gephyrin fragments. In our cell culture model, we observed a robust increase in gephyrin cleavage following OGD, evident from the increase in the 45-kDa fragment and a reduction in the full-length 100-kDa fragment, which was readily blocked by the calpain inhibitor, MDL-28170 (Calp-i) (Figure 7A). We observed similar results in the CA/CPR mice compared to sham controls (Figure S6A). To determine whether gephyrin cleavage coincides with removal of gephyrin from synaptic sites during OGD (between 10 and 15 min; Figures 2A and 2C), we measured gephyrin cleavage kinetics within the first 15 min of an OGD insult (Figure 7B). Unlike with γ2-S327 dephosphorylation, there was no significant gephyrin cleavage within the first 6 min of the insult. However, gephyrin cleavage was significantly increased at 9 min post-OGD onset, with maximal levels of cleavage at 12 and 15 min (Figure 7B). This coincides with the timing of gephyrin shrinkage and removal from GABAergic synaptic sites (Figures 2A, 2C, 3C, and 3D). To test whether calpain activation was required for the reorganization of gephyrin nanoscale architecture that accompanies its loss from the synapse (Figures 3C and 3D), we used 3D-SIM and segmentation analysis following OGD exposure for 20 min, in the absence or presence of Calp-i (Figure 7C). As shown in Figure 3, gephyrin compartment volume, SSD volume, and SSD number were decreased following 20 min of OGD compared to controls (Figures 7D and S6D). However, this decrease was blocked upon calpain inhibition (Figures 7D and S6D). Interestingly, blocking gephyrin reorganization with calpain partially rescued $GABA_AR$ nanoscale clustering at inhibitory synapses, further supporting the interdependence of both the receptor and scaffold for proper synapse organization.

Author Manuscript Author Manuscript Author Manuscript Author Manuscript

Calcineurin and calpain inhibition are both required to preserve inhibitory synaptic structure following OGD

OGD-induced gephyrin cleavage followed a similar timeline to gephyrin declustering and was prevented by blocking calpain activation. Given the role of gephyrin in clustering synaptic $GABA_ARs$, we then asked whether calpain inhibition might be sufficient to prevent OGD-induced synapse disassembly. We performed gephyrin, $GABA_AR$, and VGAT cluster analysis following a 30-min OGD insult, with either CsA or Calp-i included alone or in combination (Figure 7E). As in Figure 5B, CaN inhibition alone preserved $GABA_AR$ cluster area and density but only partially restored gephyrin clustering (Figure 7F). In contrast, calpain inhibition alone fully prevented OGD-induced gephyrin shrinkage and removal from synapses but only partially restored $GABA_ARs$ at synapses (Figure 7F). Only dual inhibition of CaN and calpain fully restored both $GABA_AR$ and gephyrin synaptic clustering following OGD (Figures 7E and 7F). CaN inhibition alone could not prevent OGD-induced gephyrin cleavage (Figure S6B). Conversely, $GABA_AR$-γ2-S327 dephosphorylation was not prevented by calpain inhibition (Figure S6C). Together, these data support the activation of two independent mechanisms to rapidly reorganize and disassemble GABAergic synapses following OGD insult: CaN-dependent dephosphorylation of synaptic $GABA_ARs$, followed by calpain-dependent cleavage of the gephyrin scaffold.

DISCUSSION

Here, we investigated the stepwise disassembly of GABAergic synapses during an excitotoxic OGD insult and delineated the signaling mechanisms that underly the nanoscale reorganization and sequential removal of $GABA_ARs$ and gephyrin from inhibitory postsynaptic sites. Most studies examining the effect of ischemia on inhibitory synapses are performed multiple hours to days following the insult, by which time synapse elimination has already taken place. This manifests in drastically reduced synapse numbers (Alicke and Schwartz-Bloom, 1995; Costa et al., 2016; Mele et al., 2014) but largely fails to capture the actual process of synapse disassembly. In contrast, here we examined the fine details of inhibitory synapse disassembly within the first 30 min of OGD and ischemia induction to define this process and the underlying mechanisms with the view that they represent the initial steps leading to impaired synaptic inhibition following excitotoxic insult. To accurately measure changes in inhibitory synapse structure, we used super-resolution 3D-SIM throughout the OGD insult. The improved spatial resolution provided by 3D-SIM makes it an ideal approach to examine synapse shrinkage, because the majority of synapses have dimensions at, or below, the resolution limit of conventional microscopy (Sigal et al., 2018). 3D-SIM revealed that inhibitory synapse disassembly in dendrites occurs in a stepwise manner: $GABA_ARs$ are lost first, along with presynaptic active zone proteins, followed by NL2 and gephyrin, and lastly by complete loss of the presynaptic terminal (Figure S7). At the presynaptic site, the active zone proteins RIM1 and bassoon are removed at a similar time point as $GABA_ARs$, indicating that the key functional synaptic components ($GABA_ARs$ and presynaptic active zone proteins) are rapidly lost following OGD onset. This is followed by delayed elimination of additional proteins with key roles in synapse structure and organization (gephyrin, NL2, and VGAT).

Author Manuscript Author Manuscript Author Manuscript Author Manuscript

We also found that $GABA_A$Rs and gephyrin undergo nanoscale architectural rearrangements following the onset of OGD. We recently showed that $GABA_A$Rs and gephyrin are organized into nanoscale SSDs at inhibitory synapses (Crosby et al., 2019). This organization is thought to be important for optimal positioning of $GABA_A$Rs near GABA release sites (Crosby et al., 2019; Yang et al., 2021), and a modular synaptic structure is postulated to underlie mechanisms of synapse growth (Crosby et al., 2019). During activity-dependent synapse growth, $GABA_A$R and gephyrin SSDs emerge at inhibitory synapses, suggesting that addition of these ‘‘building blocks’’ could drive synapse growth and strengthening during plasticity (Crosby et al., 2019). Conversely, we now show that both $GABA_A$R and gephyrin SSDs shrink and are removed from the synapse during pathogenic synaptic elimination. The robust change in $GABA_A$R nanoscale organization following OGD onset, reflected in reduced $GABA_A$R SSD number and volume, likely represents an initial step of inhibitory synapse disassembly. This effect is paralleled in dSTORM and PLA experiments, which indicate that $GABA_A$Rs rapidly decluster from gephyrin and their density decreases at the synapse at this same time point after OGD induction. This suggests that SSD shrinkage and removal is due to $GABA_A$Rs dispersing from the synapse, and likely from the SSDs themselves, although this remains to be shown. There was also a significant reduction in gephyrin SSD number and volume at later time points post-OGD insult, suggesting that SSD shrinkage and removal may be a common mechanism to reduce the size of synaptic compartments. Crucially, we identified that CaN and calpain activity are required for these sequential changes to $GABA_A$R and gephyrin nanoscale architecture, respectively, providing the mechanistic underpinning for the fine structural changes that occur leading to synapse shrinkage. Interestingly, loss of $GABA_A$R and gephyrin SSDs at somatic inhibitory synapses progressed differently compared to their dendritic counterparts: $GABA_A$R and gephyrin SSDs shrank and were removed from the synapses in parallel and more gradually over the duration of the OGD insult (Figures 3E–3H). These striking differences in synapse shrinkage may be due to distinct molecular and mechanistic differences between these synapse types, which could impact their nanoscale organization and stability. Future studies will delineate these mechanisms further and decipher whether alterations to inhibitory synapse nanoscale organization are common to multiple forms of excitotoxic insult and more transient forms of plasticity.

Our data show that ~50% synapses were eliminated following 25 min of OGD (Figure 2C), and this rose to ~80% following 2 h of reperfusion (Figures S1E and S1F), indicating that not all inhibitory synapses are disassembled and eliminated at the same rate. This could be for several reasons, including diverse synaptic proteomes, different size and structural complexity, the degree of synapse maturity, and/or the identity of the innervating interneuron subtype (Favuzzi and Rico, 2018; Sassoè-Pognetto et al., 2011). Here, we describe mechanisms facilitating the elimination of VGAT-positive inhibitory synapses that contain γ2/α1-$GABA_A$Rs. However, it is likely that ischemic insult also impacts extrasynaptic $GABA_A$Rs (γ2/α5) and tonic inhibition. Indeed, increased α5-mediated tonic inhibition impairs excitatory LTP at chronic time points following middle cerebral artery occlusion models of stroke (Orfila et al., 2019). Whether OGD similarly impacts extrasynaptic receptors at the acute time points studied here represents important future experiments.

Author Manuscript Author Manuscript Author Manuscript Author Manuscript

$GABA_AR$s undergo enhanced endocytosis within 30 min of OGD induction (Mielke and Wang, 2005; Smith et al., 2012), although the mechanism of $GABA_AR$ synaptic dispersal during OGD was undefined prior to our findings here. Our 3D-SIM and dSTORM imaging showed that rapid, OGD-induced rearrangements of $GABA_AR$ nanoscale architecture and declustering from the synapse were dependent on CaN activity. Furthermore, we found that $GABA_AR$ synaptic declustering from the synapse during OGD relied on CaN-dependent dephosphorylation of S327 on the $GABA_AR$-γ2 subunit. This is similar to the process of $GABA_AR$ declustering immediately following non-pathogenic NMDAR stimulation, where the $GABA_AR$-g2-S327 site is also dephosphorylated by CaN, enabling $GABA_AR$ declustering from the synapse (Muir et al., 2010). Likewise, $GABA_AR$ synaptic dispersal during an *in vitro* model of status epilepticus is also CaN dependent (Eckel et al., 2015). Together, this suggests that both pathogenic synapse elimination and NMDAR-driven synapse depression share the similar initial mechanism of CaN-dependent receptor declustering. However, $GABA_AR$ declustering in non-pathogenic depression is transient: $GABA_AR$s are not internalized and are quickly re-clustered back at synaptic sites (Muir et al., 2010). This is in stark contrast to OGD, where $GABA_AR$s are endocytosed (Smith et al., 2012), and their loss from the surface is permanent, as shown in our reperfusion experiments (Figures S1E and S1F). In line with this, we show that $GABA_AR$ surface levels are reduced following 30 min OGD, and this surface downregulation can be prevented by CaN inhibition, indicating that OGD-driven, CaN-dependent $GABA_AR$ declustering is upstream of receptor endocytosis.

The delayed removal of gephyrin from dendritic synapses suggested that gephyrin loss may be independently regulated from receptor declustering. Accordingly, CaN inhibition or mutation of $GABA_AR$-γ2-S327 only partially retained gephyrin at synaptic sites following OGD. This is likely due to the stabilization of residual gephyrin by the fully clustered $GABA_AR$s and highlights that, in addition to gephyrin scaffolding the $GABA_AR$s, the receptors are also important for clustering gephyrin itself (Essrich et al., 1998; Panzanelli et al., 2011; Schweizer et al., 2003). This also emphasizes the ability of $GABA_AR$s to cluster at synapses with very little gephyrin present (Fischer et al., 2000; Kneussel et al., 2001; Lévi et al., 2004) and supports the crucial roles of alternative inhibitory scaffolds, including LHFPL4/GARLH and GIT1 (Davenport et al., 2017; Smith et al., 2014; Yamasaki et al., 2017). Interestingly, we found the critical adhesion protein, NL2, is removed gradually from the synapse over the duration of OGD, compared with $GABA_AR$s or gephyrin. Like $GABA_AR$s, NL2 undergoes trafficking and likely lateral diffusion in the plasma membrane (Chamma et al., 2016; Halff et al., 2019), allowing some to be lost from the synapse rapidly following OGD onset. However, it is also likely that a significant proportion of NL2 is part of stable complexes within the synapse and therefore may be removed over longer time scales. Further nanoscale and dynamic imaging will be required to investigate these possibilities.

Under physiological conditions, calpain activity influences gephyrin clustering (Tyagarajan et al., 2011, 2013), and gephyrin is known to be cleaved several hours to days following excitotoxic insult (Costa et al., 2016; González, 2019). We found that calpain activity drives rapid gephyrin nanoscale reorganization and removal from synapses at the early stage following OGD onset, and this loss of synaptic gephyrin is paralleled by increased

Author Manuscript Author Manuscript Author Manuscript Author Manuscript

gephyrin cleavage. Delayed gephyrin cleavage and synaptic removal could be due to a delay in calpain activation, which requires the generation of mM Ca^{2+} concentrations (Goll et al., 2003; Lai et al., 2014), whereas the Ca^{2+} threshold for CaN activation is much lower (<1 μM) and could explain its rapid activation (Quintana et al., 2005). Alternatively, the localization of calpain relative to synaptic sites is unknown, indicating that it may need to be actively recruited to GABAergic synaptic sites to engage in gephyrin cleavage (Curcio et al., 2016; Perlmutter et al., 1990). In contrast to OGD-mediated gephyrin removal, gephyrin clustering during non-pathogenic NMDAR receptor stimulation is largely unaltered and at best transiently modified (Bannai et al., 2009; Muir et al., 2010). This could be due to dynamics of Ca^{2+} homeostasis, where the rise of intracellular Ca^{2+} is transient, spatially restricted, and relieson Ca^{2+}buffering mechanisms to prevent Ca^{2+}overload (Berridge et al., 2003; Bodalia et al., 2013; Matthews et al., 2013).

In summary, our data directly show that OGD-induced $GABA_AR$ and gephyrin nanoscale reorganization and removal from inhibitory synaptic sites is temporally regulated through two independent signaling mechanisms. To fully retain both $GABA_ARs$ and gephyrin at synaptic sites after OGD induction, inhibition of both CaN and calpain activity is required. Unlike nonpathological synaptic depression, excitotoxicity drives long-lasting effects, resulting in persistent synapse disassembly and elimination. This removal of synaptic $GABA_ARs$, gephyrin, and presynaptic proteins may eliminate an existing blueprint for the GABAergic synaptic site, making it impossible to re-establish these synapses at precise locations following the insult. More broadly, GABAergic synapse elimination, altered $GABA_AR$ trafficking, and reduced synaptic inhibition are all key hallmarks that contribute to hyperexcitability following multiple forms of excitotoxic insult, including ischemia (Kelley et al., 2008; Mele et al., 2014; Mielke and Wang, 2005; Zhan et al., 2006), epilepsy (Blair et al., 2004; El-Hassar et al., 2007; Goodkin et al., 2005; Naylor et al., 2005), and traumatic brain injury (Almeida-Suhett et al., 2015). Thus, the inhibitory synapse disassembly mechanisms described here could be responsible for inhibitory synapse elimination and impaired synaptic inhibition in a number of acute excitotoxic brain disorders.

Limitations of the study

Here, we have studied inhibitory synapse elimination and the nanoscale synaptic alterations that underlie this process in an *in vitro* model of global ischemia (OGD). We paralleled these experiments to show similar inhibitory synapse loss in a CA/CPR *in vivo* global ischemia model. The CA/CPR insult revealed similar results as OGD; however, comparisons between the two models are limited without further characterization (due to timing post-insult and differences in reperfusion). Although technically challenging, analysis of inhibitory synapse nanoscale architecture following CA/CPR would further validate the mechanisms of synapse disassembly we presented *in vitro*.

Author Manuscript Author Manuscript Author Manuscript Author Manuscript

STAR★METHODS

RESOURCE AVAILABILITY

Lead contact—Any additional information or enquiries about reagents and resources should be directed to the Lead contact, Katharine R. Smith (katharine.r.smith@cuanschutz.edu).

Materials availability—The transfer of plasmids generated for this study will be made available upon request. A Materials Transfer Agreement may be required.

Data and code availability—No standardized datatypes are reported in this paper. All data reported in this paper will be shared by the lead contact upon request. This paper does not report original code. Any additional information required to reanalyze the data reported in this paper is available from the lead contact upon request.

EXPERIMENTAL MODEL AND SUBJECT DETAILS

All animal procedures are in accordance with the National Institutes of Health (NIH) *Guide for the Care and Use of Laboratory Animals* and approved with the Institutional Animal Care and Use Committee at the University of Colorado, Denver Anschutz Medical Campus (CU-AMC). Animals were housed at the Animal Resource Center (CU-AMC) and were routinely monitored for general health, cage changes, feedings and overcrowding. Timed pregnant Sprague-Dawley rats were supplied by Charles River Labs and neonatal pups were used postnatal day 0–1 as described below. Male and female C57BL/6 adult mice (8–10 weeks) were supplied by Charles River Labs.

Dissociated Hippocampal Cultures—As previously described (Crosby et al., 2019; Rajgor et al., 2020), primary neuronal cultures were prepared from dissected hippocampi of mixed sex neonatal rat pups (postnatal day 0–1) and dissociated in papain. Neurons were seeded in MEM and 10% FBS containing penicillin/streptomycin either onto 18mm #1.5 glass coverslips at a density of 150,000–200,000 cells or 6-cm dishes at 3,000,000 cells coated with poly-D-lysine. MEM was replaced 24h following plating with Neurobasal (NB) media (GIBCO) supplemented with B27 (GIBCO) and 2 mM Glutamax. Feedings were performed every 5 days by removing half the media and replacing with new NB media. To limit growth of actively dividing cells, mitotic inhibitors (uridine fluoro deoxyuridine) were added at day 5. Cultures were maintained at 37°C, 5% CO_2 for 15–18 days prior to experiments.

Cardiac Arrest and Cardiopulmonary Resuscitation Animal Model—C57BL/6 mice (8–10 weeks old, both sexes) were subject to cardiac arrest and cardiopulmonary resuscitation (CA/CPR) or sham treatments as previously described (Deng et al., 2017). Mice were anesthetized (3% isoflurane), intubated and placed on a ventilator set at 160 breaths per min. Vitals were monitored by ECG and body temperature was maintained at 37.5°C ± 0.2C. KCl injection via the jugular catheter induced asystolic CA for 6–7 min. CPR was induced by a slow injection of epinephrine (16 μg epinephrine/mL, 0.9% saline), chest compression (~300 per min) and ventilation of 100% O_2. If spontaneous recirculation

Author Manuscript Author Manuscript Author Manuscript Author Manuscript

was not achieved by 3-min of CPR, the animal was omitted from the study. Vitals were monitored up to 15 min following resuscitation, prior to harvesting samples (Buonarati et al., 2020; Deng et al., 2017).

METHOD DETAILS

Oxygen Glucose Deprivation (OGD) treatments *in vitro*—OGD was induced in DIV15–18 hippocampal neuronal cultures with a HEPES-buffered solution (25mM HEPES, pH 7.4, 140mM NaCl, 5mM KCl, 2mM $CaCl_2$, 1mM $MgCl_2$, and 10mM sucrose or supplemented with 10mM glucose for control). OGD-HEPES solution was placed in an anaerobic workstation at 37°C, 95% N_2 and 5% CO_2 (Bugbox Plus, Baker Co) 24–48 hours prior to treatments to allow deoxygenation. Neuronal cultures were washed twice and incubated with OGD-HEPES solution in the anoxic chamber prior to being harvested or fixed at specific time points as stated in each figure. Control neurons were incubated at 37°C, 5% CO_2 with Control-HEPES solution and harvested or fixed at similar time points as OGD conditions. For reperfusion experiments, HEPES solution was replaced with conditioned media and placed in the aerobic incubator for specified time. Inhibitors were used at the following final concentration: Cyclosporin A (CsA) – 5 μM; FK506 – 5 μM; MDL-28170 (Calp-i) – 100 μM; DMSO – 1:1000 dilution; APV – 50 μM.

Immunocytochemistry (ICC)—Neuronal cultures grown on coverslips were fixed in 4% PFA solution (4% sucrose, 1X PBS and 50mM HEPES (pH 7.5)) for 5 min at RT. Coverslips were blocked in 5% BSA, 2% Normal Goat Serum (NGS) and 1X PBS at RT for 30 min. Surface $GABA_AR$-γ2 (1:500 Synaptic Systems Guinea Pig – 224004), $GABA_AR$-α1 (1:500 Synaptic Systems Rabbit – 224203) and SEP-tagged $GABA_AR$- γ2 (antiGFP, 1:1000 Invitrogen Rabbit – A11122) staining was performed under nonpermeabilized conditions in blocking solution for 1 hour at RT. Coverslips were washed for 5 min (3X) in PBS followed by permeabilization in 0.5% NP-40 for 2 mins and blocked at RT for 30 min. Gephyrin mAb7a (1:500 Synaptic Systems Mouse – 147011), Gephyrin 3B11 (1:600 Synaptic Systems Mouse – 147111), VGAT (1:1000 Synaptic Systems Rabbit – 131003 or Guinea Pig – 131004), RIM1 (1:150 Synaptic Systems Rabbit – 140003), Bassoon (1:1000 Synaptic Systems Guinea Pig – 141004), Neuroligin 2 (1:500 Synaptic Systems Mouse – 129511), GAD1/67 (1:750 Synaptic Systems Rabbit – 198003) and $GABA_AR$-β3 (1:1000 Neuromab Mouse – 75149) staining was performed in blocking solution for 1 hour followed by 5 min washes (3X). Coverslips were incubated with appropriate secondary antibodies (1:1000 ThermoFisher Alexa – Fluor 488, 568 and 647) for 1 hr in blocking solution. Coverslips were washed for 5 min (3X) before being mounted on microscope slides with ProLong Gold mounting media (Thermofisher).

Immunohistochemistry (IHC)—Following CA/CPR or sham treatments, mice were anesthetized and transcardially perfused with ice cold PBS followed by 4% PFA. Brains were harvested for post-fixation in 4% PFA at 4°C for 24 hours and were transferred to cryoprotection solution (30% sucrose and 0.1% Sodium azide in PBS) for storage until sectioning. Frozen coronal sections (30–50 μm) were cut using a cryostat and stored in cryoprotection solution. Free floating sections were washed for 15 min (3X) in PBS at RT and permeabilized (5% BSA, 5% NGS, 0.5% Triton X-100 and 1X PBS) at RT for

Author Manuscript Author Manuscript Author Manuscript Author Manuscript

5–6 hours on a rocker. Slices were incubated with $GABA_AR$ γ2 (1:500 Synaptic Systems Guinea Pig 224004), gephyrin (1:500 Synaptic Systems Mouse 147011) and VGAT (1:1000 Synaptic Systems Rabbit – 131003) antibodies in permeabilization solution overnight at 4°C on a rocker. Slices were washed for 20 min in PBS (4X) and incubated with appropriate secondary antibodies (1:1000 ThermoFisher Alexa Fluor 488, 568 and 647) for 2 hours in blocking solution. Prior to mounting with ProLong Gold, slices were washed for 20 min in PBS (4 times).

Proximity Ligation Assay (PLA)—PLA was performed using the DuoLink *in situ* red PLA mouse/rabbit kit (Sigma) as described in Rajgor et al. (2020) under permeabilized conditions, unless stated. The $GABA_AR$-α1 subunit (1:500 Synaptic Systems Rabbit - 224203) and gephyrin (1:500 Synaptic Systems Mouse - 147011) antibodies were used at the same dilution as with ICC. PLA positive puncta reactivity was imaged on the confocal microscope (see below) and measured as density per 10 mm in ImageJ. PLA controls include reactions under nonpermeabilized conditions to exclude targets with an intracellular epitope or excluding a single primary antibody (e.g., no $GABA_AR$-α1 or gephyrin primary antibody).

Transfections—DNA transfections were performed at DIV 15–16 and allowed to express for 18–24 hours before treatments. DNA (~300ng/well) was incubated with Lipofectamine 2000 (Invitrogen) for 20–25 min to allow complex formation. Transfection mix was applied to neuronal cultures for 1.5–2 hours before replacing with conditioned media. For DNA constructs, refer to key resources table.

QUANTIFICATION AND STATISTICAL ANALYSIS

Image Acquisition and Data analysis

Confocal microscopy: Confocal images were acquired on a Zeiss Axio Observer.Z1 upright microscope equipped with a Yokogawa CSU-X1 spinning disk unit; a 63X oil immersion objective (Plan-Apo/1.4 NA); an Evolve 512 EM-CCD camera (Photometrics) with 16-bit range; and Slide-Book 6.0. Images were attained at 0.3 μm intervals (4 μm Z stack projection). Cluster analysis was performed using ImageJ (NIH) by selecting regions of interest (ROIs) to differentiate between dendritic and somatic compartments. A user-based threshold was determined by sampling several images per condition across all conditions and clusters were defined as a minimum size of 0.05 μm^2. For *in vitro* experiments, ROIs were delineated by tracing along dendrites or around the soma. Density was calculated by measuring the length of dendrites analyzed (per 10 μm) or the area of the soma (per μm^2). Three independent experiments analyzed 10–12 neurons per condition for a total of 30–36 neurons. For *in vivo* experiments, the CA1 hippocampus was identified by VGAT staining of the pyramidal cell layer (PCL). ROIs captured both the PCL and *Stratum radiatum* in the same frame, and different user-based thresholds were used for the cell bodies and dendrites. Density was calculated by dividing the number of clusters by the ROI area (per μm^2). A minimum of 5 animals per condition were imaged, and two slices per animal analyzed. All confocal analysis was performed blind to experimental condition.

Author Manuscript Author Manuscript Author Manuscript Author Manuscript

3D Structured Illumination Microscopy (3D-SIM): Images were acquired with a Nikon SIM-E Structured Illumination super-resolution microscope equipped with a 100x, 1.49 NA objective; an ORCA-Flash 4.0 sCMOS camera (Hamamatsu); and Nikon Elements software. To maximize signal to noise and reduce photobleaching, acquisition conditions and camera integration time were set in a similar manner to Crosby et al. (2019). On average, 8–15 ROIs (individual synapses) were manually selected per neuron (4–5 neurons) for each condition, with a biological replicate of 3 neuronal cultures for a total of 130–180 synapses (12–15 neurons) per condition. Synapses were within the entire Z stack, and each selection was based off VGAT positive staining since presynaptic terminals are most stable component of the synapse. A high throughput pipeline for analysis is as follows: synapses were processed by background subtraction (ImageJ), image segmentation (split-Bregman/MOSAIC suite (Paul et al., 2013; Rizk et al., 2014)) and geometric analysis (MATLAB) as further detailed in Crosby et al., 2019. For image segmentation, the following parameters were utilized: ‘Subpixel segmentation’, ‘Exclude Z edge’, Local intensity estimation ‘Medium’, Noise Model ‘Gauss’. All 3D-SIM imaging analysis was performed blind to experimental condition.

Distribution analysis of 3D-SIM total synapse volumes: The 3D-SIM analysis code automatically generates a total synapse volume (μm^3) for each synapse, which computes its size based off all 3 markers (Gephyrin, $GABA_AR$ and VGAT). All synapse volumes were collected for control or OGD 25 treatments and were fit with probability distributions describing a normal distribution and a mix of two normal distributions using MATLAB’s maximum likelihood estimator function ‘mle’. The model for normal distribution was defined using MATLAB’s ‘normpdf’ function, setting the parameter for mu and sigma: ‘@(x,mu,sigma) normpdf(x,mu,sigma);’

The model for a mix of two normal distributions was defined with five parameters: ‘@(x,p,mu1,mu2,sigma1,sigma2)...

$$p * \text{normpdf}(x, mu1, sigma1) + (1 - p) * \text{normpdf}(x, mu2, sigma2);'$$

where p is the probability of distribution 1. Errors were calculated by taking the volume data and creating a series of histogram bin counts using ‘histcounts’ with normalization set to ‘pdf,’ the resulting values were assigned to the variable *y*. *yhat* was determined by calculating the PDF based on the fitting model, using the returned parameters and an xgrid the same length as the binned data. The resulting residuals (*yhat* – *y*) were then used to calculate the root mean squared error (RMSE) and the sum of squared residuals (SSR). Model suitability was determined using a F-test function available on MATLAB File Exchange (Conder, 2021). The output of this function, *p*, is the probability (0 – 1) that the improvement in fit with a more complex model is because of the additional fit parameters rather than model suitability (smaller values indicate that the mixture model is more appropriate than the single distribution model).

dSTORM: Images were acquired on a Zeiss Elyra P.1 TIRF microscope equipped with a Zeiss alpha Plan-Apochromat TIRF 100x/1.6 NA oil objective; tube lens for an additional

Author Manuscript Author Manuscript Author Manuscript Author Manuscript

factor of 1.6x magnification; and quad-band dichroic (405/488/561/642). For both the CF568 and Alexa647 dyes, an Andor iXon+ EMCCD camera captured a sequential time-series of 20,000 frames each at a gain setting of 100 with an integration time of 18ms. Image size was 256X256 pixels, with a pixel size of 100 nm xy. Alexa-647 molecules were ground-state depleted and imaged with a 100mW 642 laser at 100% AOTF transmission in ultra-high-power mode (condensed field of illumination), corresponding to approximately 1.4W/cm^2. Emission light passed through a LP 655 filter. CF-568 molecules were ground-state depleted and imaged with a 200mW 561 laser at 100% AOTF transmission in ultra-high-power mode, corresponding to approximately 2.5W/cm^2. Emission light was passed through a BP 570–650 + LP 750 filter. For each dye, ground-state return was elicited by continuous illumination with a 50mW 405 laser at 0.01 to 0.1% AOTF transmission.

dSTORM Image processing: Localizations from dye emitters was performed using the ThunderSTORM ImageJ plugin (Ovesný et al., 2014). Image filtering was done with the Wavelet filter setting, with a B-Spline order of 3 and scale of 2.0. A first pass approximate localization of molecules was achieved with by finding local maximum with a peak intensity threshold of 3*std (Wave.F1) and 8-neighborhood connectivity. Weighted least-squares fitting of the PSF to achieve sub-pixel localizations was achieved by use of an integrated Gaussian with a fitting radius of 4 pixels and an initial sigma of 1.2. Localizations were filtered based on the attributes of uncertainty (< 20 nm), sigma (50 – 150 nm), and intensity (< 10000 for CF568 and < 15000 for Alx647). Localizations within 50 nm were merged with a frame-gap allowance of 1. Drift correction was performed using the built-in cross-correlation based method in the ThunderSTORM plugin. Channel registration was performed using custom-written MATLAB scripts and was based on multi-colored bead acquisitions taken at the start of each experiment.

STORM Analysis: Individual synapses were manually selected from a composite SR/WF image and ROI coordinates were recorded with a custom ImageJ macro. The gephyrin boundary region was segmented using a coordinate-by-coordinate density calculation. Because labeling density could vary greatly, the thresholding parameter was determined from the overall density range of the ROI. Localizations with a local-density in the lower 10% of that range were considered to be outside of the synaptic region/clusters. Boundaries for these regions were delineated using MATLAB's alphaShape function, with an α value of 100. Only regions with an area of 1.5e3 nm^2 or greater were considered for analysis. The synaptic boundary was delineated by determining the number of gephyrin localizations per nm^2 that were within the delineated synaptic boundary. The receptor density ratio ($GABA_AR$ synaptic enrichment) was determined by delineating a uniform-sized ROI (1 μm^2) around each gephyrin boundary and calculating the ratio of the density (localizations per μm^2) of the receptor within the boundary to the overall density of the receptor within the entire ROI. Due to high variability across different culture sets, the receptor density ratio for each experiment was normalized using the median value of the control samples for that experiment (Figure 5F only). All dSTORM analysis was performed blinded to experimental condition.

Author Manuscript Author Manuscript Author Manuscript Author Manuscript

Surface biotinylation—As previously described (Smith et al., 2014), hippocampal cultures ($3X10^6$ cells) were placed on ice to block the endocytic machinery and treated with biotin (Pierce Sulfo-NHS-LC-Biotin) at 0.5mg/mL (in PBS+1mM $CaCl_2$+1mM $MgCl_2$) for 15 min. Neurons were quenched with BSA (1mg/mL) in PBS+ $CaCl_2$+ $MgCl_2$ solution for 15 min; harvested in RIPA buffer (50mM Tris pH 7.5, 1mM EDTA, 2mM EGTA, 150mM NaCl, 1% NP-40, 0.5% DOC, 0.1% SDS, 50mM NaF, 1mM Na_3VO_4 and protease inhibitor (Complete Mini, EDTA-free, Roche)); and permeabilized for 1 hour. Debris was pelleted at 4°C at 15,000 rpm for 10 min. 10% of the supernatant was collected for the total protein input and the remainder was incubated with 25 μL Ultralink Immobilized NeutrAvidin 50% slurry (Pierce) for 2 hours at 4°C. Beads were washed 3X with high salt RIPA (350mM NaCl) and analyzed by western blotting. The surface levels were normalized to the 10% input of total protein.

Western blotting—Cell lysates were harvested in RIPA buffer (see above) with protease inhibitor (Roche) and phosphatase inhibitor cocktail 3 (Sigma). Samples were solubilized for 20 mins and centrifuged at max speed for 10 mins. Samples were denatured with a 4X sample buffer (62.5mM Tris pH 6.8, 2% SDS, 25% glycerol, 0.01% Bromophenol Blue and 10% beta-2-mercaptoethanol) and heated at 95°C for 5 mins. Protein lysates were resolved on a 10% SDS-PAGE gel and transferred to PVDF membrane in a wet apparatus. Blots were blocked in either 5% milk (TBS-T) or 5% BSA (TBS-T) for phospho-specific antibodies and probed with primary antibody overnight at 4°C with the following: $GABA_AR$-γ2 (1:1000 Neuromab 75442), $GABA_AR$-β3 (1:5000 Neuromab 75149), $GABA_AR$-α1 (1:2000 Neuromab 75136), $GABA_AR$-γ2 pS327 (1:1000 Abcam 73183), gephyrin (1:20,000 Synaptic Systems 147111) and GAPDH (1:40,000 GeneTex 627408). Blots were washed for 10-min (3X) followed by incubation with secondary HRP-conjugated antibodies (1:10,000 Millipore) at room temperature for 1 hour. ECL western blotting substrates were used to visualize protein bands and densitometry measurements were performed in ImageJ. Total protein was normalized to GAPDH from the same gel. Phosphorylation levels were normalized to total protein levels from the same gel. Blots were stripped and re-probed for different markers.

All statistical analysis was performed in PRISM 9 software. Specific details such as statistical test used, exact value of n, definition of center and/or dispersion and precisions measures (SEM) are outlined in each figure legend corresponding to the data.

Supplementary Material

Refer to Web version on PubMed Central for supplementary material.

ACKNOWLEDGMENTS

This work was supported by a Brain and Behavior Research Foundation NARSAD Young Investigator Award, a Brain Research Foundation Seed Grant, an AHA Career Development Award, and grant R01MH119154 to K.R.S. J.D.G. was supported by grant T32GM763540, an AHA Predoctoral Fellowship (19PRE34380542), and an NIH Blueprint Diversity Specialized Predoctoral to Postdoctoral Advancement in Neuroscience (D-SPAN) Award (FNS120640A). N.Q. and P.H. were supported by grants R01NS046072 and R01NS092645. M.L.D. was supported by grants R01NS040701 and R01123700. M.J.K. was supported by grant R35NS116879. S.L.S. was supported by grant F32MH123053. We thank Dominik Stich for assisting with the dSTORM imaging, which was performed at the University of Colorado Anschutz Medical Campus Advanced Light Microscopy Core, supported in part by

Author Manuscript Author Manuscript Author Manuscript Author Manuscript

Rocky Mountain Neurological Disorders Core grant number P30 NS048154 and by Diabetes Research Center grant number P30 DK116073. Contents are the authors' sole responsibility and do not necessarily represent official NIH views.

REFERENCES

Alicke B, and Schwartz-Bloom RD (1995). Rapid down-regulation of GABAA receptors in the gerbil hippocampus following transient cerebral ischemia. J. Neurochem 65, 2808–2811. [PubMed: 7595583]

Almeida-Suhett CP, Prager EM, Pidoplichko V, Figueiredo TH, Marini AM, Li Z, Eiden LE, and Braga MF (2015). GABAergic interneuronal loss and reduced inhibitory synaptic transmission in the hippocampal CA1 region after mild traumatic brain injury. Exp. Neurol 273, 11–23. [PubMed: 26238734]

Arancibia-Cárcamo IL, Yuen EY, Muir J, Lumb MJ, Michels G, Saliba RS, Smart TG, Yan Z, Kittler JT, and Moss SJ (2009). Ubiquitin-dependent lysosomal targeting of GABA(A) receptors regulates neuronal inhibition.Proc. Natl. Acad. Sci. USA 106, 17552–17557. [PubMed: 19815531]

Bannai H, Lévi S, Schweizer C, Inoue T, Launey T, Racine V, Sibarita J-B, Mikoshiba K, and Triller A. (2009). Activity-dependent tuning of inhibitory neurotransmission based on GABAAR diffusion dynamics. Neuron 62, 670–682. [PubMed: 19524526]

Bannai H, Niwa F, Sherwood MW, Shrivastava AN, Arizono M, Miyamoto A, Sugiura K, Lévi S, Triller A, and Mikoshiba K. (2015). Bidirectional control of synaptic GABAAR clustering by glutamate and calcium. Cell Rep.13, 2768–2780. [PubMed: 26711343]

Barberis A. (2020). Postsynaptic plasticity of GABAergic synapses. Neuropharmacology 169, 107643.

Battaglia S, Renner M, Russeau M, Come E, Tyagarajan SK, and Lévi S. (2018). Activity-dependent inhibitory synapse scaling is determined by gephyrin phosphorylation and subsequent regulation of $GABA_A$ receptor diffusion. eNeuro 5, ENEURO.0203-17.2017.

Berridge MJ, Bootman MD, and Roderick HL (2003). Calcium signalling: dynamics, homeostasis and remodelling. Nat. Rev. Mol. Cell Biol 4, 517–529. [PubMed: 12838335]

Blair RE, Sombati S, Lawrence DC, McCay BD, and DeLorenzo RJ (2004). Epileptogenesis causes acute and chronic increases in GABAA receptor endocytosis that contributes to the induction and maintenance of seizures in the hippocampal culture model of acquired epilepsy. J. Pharmacol. Exp. Ther 310, 871–880. [PubMed: 15084648]

Bodalia A, Li H, and Jackson MF (2013). Loss of endoplasmic reticulum Ca2+ homeostasis: contribution to neuronal cell death during cerebral ischemia. Acta Pharmacol. Sin 34, 49–59. [PubMed: 23103622]

Buonarati OR, Cook SG, Goodell DJ, Chalmers NE, Rumian NL, Tullis JE, Restrepo S, Coultrap SJ, Quillinan N, Herson PS, and Bayer KU (2020). CaMKII versus DAPK1 binding to GluN2B in ischemic neuronal cell death after resuscitation from cardiac arrest. Cell Rep. 30, 1–8.e4. [PubMed: 31914378]

Chamma I, Levet F, Sibarita JB, Sainlos M, and Thoumine O. (2016). Nanoscale organization of synaptic adhesion proteins revealed by single-molecule localization microscopy. Neurophotonics 3, 041810.

Chiu CQ, Barberis A, and Higley MJ (2019). Preserving the balance: diverse forms of long-term GABAergic synaptic plasticity. Nat. Rev. Neurosci20, 272–281. [PubMed: 30837689]

Conder J. (2021). F-Test. https://www.mathworks.com/matlabcentral/fileexchange/41775-f-test.

Costa JT, Mele M, Baptista MS, Gomes JR, Ruscher K, Nobre RJ, de Almeida LP, Wieloch T, and Duarte CB (2016). Gephyrin cleavage in in vitro brain ischemia decreases GABAA receptor clustering and contributes to neuronal death. Mol. Neurobiol 53, 3513–3527. [PubMed: 26093381]

Crosby KC, Gookin SE, Garcia JD, Hahm KM, Dell'Acqua ML, and Smith KR (2019). Nanoscale subsynaptic domains underlie the organization of the inhibitory synapse. Cell Rep. 26, 3284–3297.e3. [PubMed: 30893601]

Curcio M, Salazar IL, Mele M, Canzoniero LM, and Duarte CB (2016). Calpains and neuronal damage in the ischemic brain: the swiss knife in synaptic injury. Prog. Neurobiol 143, 1–35. [PubMed: 27283248]

Author Manuscript Author Manuscript Author Manuscript Author Manuscript

Davenport EC, Pendolino V, Kontou G, McGee TP, Sheehan DF, López-Doménech G, Farrant M, and Kittler JT (2017). An essential role for the tetraspanin LHFPL4 in the cell-type-specific targeting and clustering of synaptic $GABA_A$ receptors. Cell Rep. 21, 70–83. [PubMed: 28978485]

Deng G, Orfila JE, Dietz RM, Moreno-Garcia M, Rodgers KM, Coultrap SJ, Quillinan N, Traystman RJ, Bayer KU, and Herson PS (2017). Autonomous CaMKII activity as a drug target for histological and functional neuroprotection after resuscitation from cardiac arrest. Cell Rep. 18, 1109–1117. [PubMed: 28147268]

Eckel R, Szulc B, Walker MC, and Kittler JT (2015). Activation of calcineurin underlies altered trafficking of a2 subunit containing GABAA receptors during prolonged epileptiform activity. Neuropharmacology 88, 82–90. [PubMed: 25245802]

El-Hassar L, Esclapez M, and Bernard C. (2007). Hyperexcitability of the CA1 hippocampal region during epileptogenesis. Epilepsia 48 (Suppl 5), 131–139. [PubMed: 17910593]

Essrich C, Lorez M, Benson JA, Fritschy J-M, and Lüscher B. (1998). Postsynaptic clustering of major GABAA receptor subtypes requires the g 2 subunit and gephyrin. Nat. Neurosci 1, 563–571. [PubMed: 10196563]

Favuzzi E, and Rico B. (2018). Molecular diversity underlying cortical excitatory and inhibitory synapse development. Curr. Opin. Neurobiol 53, 8–15. [PubMed: 29704699]

Fischer F, Kneussel M, Tintrup H, Haverkamp S, Rauen T, Betz H, and Wässle H. (2000). Reduced synaptic clustering of GABA and glycine receptors in the retina of the gephyrin null mutant mouse. J. Comp. Neurol 427, 634–648. [PubMed: 11056469]

Fritschy JM (2008). Epilepsy, E/I balance and GABA(A) receptor plasticity. Front. Mol. Neurosci 1, 5. [PubMed: 18946538]

Gao R, and Penzes P. (2015). Common mechanisms of excitatory and inhibitory imbalance in schizophrenia and autism spectrum disorders. Curr. Mol. Med 15, 146–167. [PubMed: 25732149]

Goll DE, Thompson VF, Li H, Wei W, and Cong J. (2003). The calpain system. Physiol. Rev 83, 731–801. [PubMed: 12843408]

González MI (2019). Calpain-dependent cleavage of GABAergic proteins during epileptogenesis. Epilepsy Res. 157, 106206.

Goodkin HP, Yeh JL, and Kapur J. (2005). Status epilepticus increases the intracellular accumulation of GABAA receptors. J. Neurosci 25, 5511–5520. [PubMed: 15944379]

Halff EF, Szulc BR, Lesept F, and Kittler JT (2019). SNX27-mediated recycling of neuroligin-2 regulates inhibitory signaling. Cell Rep. 29, 2599–2607.e6. [PubMed: 31775031]

Heilemann M, van de Linde S, Schüttpelz M, Kasper R, Seefeldt B, Mukherjee A, Tinnefeld P, and Sauer M. (2008). Subdiffraction-resolution fluorescence imaging with conventional fluorescent probes. Angew. Chem. Int. Ed. Engl 47, 6172–6176. [PubMed: 18646237]

Kelley MH, Taguchi N, Ardeshiri A, Kuroiwa M, Hurn PD, Traystman RJ, and Herson PS (2008). Ischemic insult to cerebellar Purkinje cells causes diminished GABAA receptor function and allopregnanolone neuroprotection is associated with GABAA receptor stabilization. J. Neurochem 107, 668–678. [PubMed: 18699862]

Kittler JT, Chen G, Honing S, Bogdanov Y, McAinsh K, Arancibia-Carcamo IL, Jovanovic JN, Pangalos MN, Haucke V, Yan Z, and Moss SJ (2005). Phospho-dependent binding of the clathrin AP2 adaptor complex to GABAA receptors regulates the efficacy of inhibitory synaptic transmission. Proc. Natl. Acad. Sci. USA 102, 14871–14876. [PubMed: 16192353]

Klausberger T, and Somogyi P. (2008). Neuronal diversity and temporal dynamics: the unity of hippocampal circuit operations. Science 321, 53–57. [PubMed: 18599766]

Kneussel M, Brandstätter JH, Gasnier B, Feng G, Sanes JR, and Betz H. (2001). Gephyrin-independent clustering of postsynaptic GABA(A) receptor subtypes. Mol. Cell. Neurosci 17, 973–982. [PubMed: 11414787]

Kowalczyk S, Winkelmann A, Smolinsky B, Förstera B, Neundorf I, Schwarz G, and Meier JC (2013). Direct binding of GABAA receptor β2 and β3 subunits to gephyrin. Eur. J. Neurosci 37, 544–554. [PubMed: 23205938]

Kuhse J, Kalbouneh H, Schlicksupp A, Mükusch S, Nawrotzki R, and Kirsch J. (2012). Phosphorylation of gephyrin in hippocampal neurons by cyclin-dependent kinase CDK5 at Ser-270 is dependent on collybistin. J. Biol. Chem 287, 30952–30966. [PubMed: 22778260]

Author Manuscript Author Manuscript Author Manuscript Author Manuscript

Lai TW, Zhang S, and Wang YT (2014). Excitotoxicity and stroke: identifying novel targets for neuroprotection. Prog. Neurobiol 115, 157–188. [PubMed: 24361499]

Lévi S, Logan SM, Tovar KR, and Craig AM (2004). Gephyrin is critical for glycine receptor clustering but not for the formation of functional GABAergic synapses in hippocampal neurons. J. Neurosci 24, 207–217. [PubMed: 14715953]

Lorenz-Guertin JM, and Jacob TC (2018). GABA type a receptor trafficking and the architecture of synaptic inhibition. Dev. Neurobiol 78, 238–270. [PubMed: 28901728]

Matthews EA, Schoch S, and Dietrich D. (2013). Tuning local calcium availability: cell-type-specific immobile calcium buffer capacity in hippocampal neurons. J. Neurosci 33, 14431–14445. [PubMed: 24005295]

Mele M, Ribeiro L, Inácio AR, Wieloch T, and Duarte CB (2014). GABA(A) receptor dephosphorylation followed by internalization is coupled to neuronal death in in vitro ischemia. Neurobiol. Dis 65, 220–232. [PubMed: 24513087]

Mele M, Costa RO, and Duarte CB (2019). Alterations in $GABA_A$-receptor trafficking and synaptic dysfunction in brain disorders. Front. Cell. Neurosci13, 77. [PubMed: 30899215]

Mielke JG, and Wang YT (2005). Insulin exerts neuroprotection by counteracting the decrease in cell-surface GABA receptors following oxygen-glucose deprivation in cultured cortical neurons. J. Neurochem 92, 103–113. [PubMed: 15606900]

Muir J, Arancibia-Carcamo IL, MacAskill AF, Smith KR, Griffin LD, and Kittler JT (2010). NMDA receptors regulate GABAA receptor lateral mobility and clustering at inhibitory synapses through serine 327 on the γ2 subunit.Proc. Natl. Acad. Sci. USA 107, 16679–16684. [PubMed: 20823221]

Mukherjee J, Kretschmannova K, Gouzer G, Maric HM, Ramsden S, Tretter V, Harvey K, Davies PA, Triller A, Schindelin H, and Moss SJ (2011). The residence time of GABA(A)Rs at inhibitory synapses is determined by direct binding of the receptor α1 subunit to gephyrin. J. Neurosci 31, 14677–14687. [PubMed: 21994384]

Naylor DE, Liu H, and Wasterlain CG (2005). Trafficking of GABA(A) receptors, loss of inhibition, and a mechanism for pharmacoresistance in status epilepticus. J. Neurosci 25, 7724–7733. [PubMed: 16120773]

Niwa F, Patrizio A, Triller A, and Specht CG (2019). cAMP-EPAC-dependent regulation of gephyrin phosphorylation and GABAAR trapping at inhibitory synapses. iScience 22, 453–465. [PubMed: 31835170]

Nusser Z, Cull-Candy S, and Farrant M. (1997). Differences in synaptic GABA(A) receptor number underlie variation in GABA mini amplitude. Neuron 19, 697–709. [PubMed: 9331359]

Oh WC, and Smith KR (2019). Activity-dependent development of GABAergic synapses. Brain Res. 1707, 18–26. [PubMed: 30439352]

Orfila JE, Grewal H, Dietz RM, Strnad F, Shimizu T, Moreno M, Schroeder C, Yonchek J, Rodgers KM, Dingman A, et al. (2019). Delayed inhibition of tonic inhibition enhances functional recovery following experimental ischemic stroke. J. Cereb. Blood Flow Metab 39, 1005–1014. [PubMed: 29283314]

Ovesný M, Krízek P, Borkovec J, Svindrych Z, and Hagen GM (2014). ThunderSTORM: a comprehensive ImageJ plug-in for PALM and STORM data analysis and super-resolution imaging. Bioinformatics 30, 2389–2390. [PubMed: 24771516]

Panzanelli P, Gunn BG, Schlatter MC, Benke D, Tyagarajan SK, Scheiffele P, Belelli D, Lambert JJ, Rudolph U, and Fritschy JM (2011). Distinct mechanisms regulate GABAA receptor and gephyrin clustering at perisomatic and axo-axonic synapses on CA1 pyramidal cells. J. Physiol 589, 4959–4980. [PubMed: 21825022]

Paul G, Cardinale J, and Sbalzarini IF (2013). Coupling image restoration and segmentation: a generalized linear model/Bregman perspective. Int. J. Comput. Vis 104, 69–93.

Pennacchietti F, Vascon S, Nieus T, Rosillo C, Das S, Tyagarajan SK, Diaspro A, Del Bue A, Petrini EM, Barberis A, and Cella Zanacchi F. (2017). Nanoscale molecular reorganization of the inhibitory postsynaptic density is a determinant of GABAergic synaptic potentiation. J. Neurosci 37, 1747–1756. [PubMed: 28073939]

Perlmutter LS, Gall C, Baudry M, and Lynch G. (1990). Distribution of calcium-activated protease calpain in the rat brain. J. Comp. Neurol 296, 269–276. [PubMed: 2358536]

Author Manuscript Author Manuscript Author Manuscript Author Manuscript

Petrini EM, and Barberis A. (2014). Diffusion dynamics of synaptic molecules during inhibitory postsynaptic plasticity. Front. Cell. Neurosci 8, 300. [PubMed: 25294987]

Petrini EM, Ravasenga T, Hausrat TJ, Iurilli G, Olcese U, Racine V, Sibarita JB, Jacob TC, Moss SJ, Benfenati F, et al. (2014). Synaptic recruitment of gephyrin regulates surface GABAA receptor dynamics for the expression of inhibitory LTP. Nat. Commun 5, 3921. [PubMed: 24894704]

Quintana AR, Wang D, Forbes JE, and Waxham MN (2005). Kinetics of calmodulin binding to calcineurin. Biochem. Biophys. Res. Commun 334, 674–680. [PubMed: 16009337]

Rajgor D, Purkey AM, Sanderson JL, Welle TM, Garcia JD, Dell'Acqua ML, and Smith KR (2020). Local miRNA-dependent translational control of $GABA_AR$ synthesis during inhibitory long-term potentiation. Cell Rep. 31, 107785.

Rizk A, Paul G, Incardona P, Bugarski M, Mansouri M, Niemann A, Ziegler U, Berger P, and Sbalzarini IF (2014). Segmentation and quantification of subcellular structures in fluorescence microscopy images using Squassh.Nat. Protoc 9, 586–596. [PubMed: 24525752]

Rust MJ, Bates M, and Zhuang X. (2006). Sub-diffraction-limit imaging by stochastic optical reconstruction microscopy (STORM). Nat. Methods 3, 793–795. [PubMed: 16896339]

Sassoè-Pognetto M, Frola E, Pregno G, Briatore F, and Patrizi A. (2011). Understanding the molecular diversity of GABAergic synapses. Front. Cell. Neurosci 5, 4. [PubMed: 21713106]

Schweizer C, Balsiger S, Bluethmann H, Mansuy IM, Fritschy J-M, Mohler H, and Lüscher B. (2003). The γ 2 subunit of GABA(A) receptors is required for maintenance of receptors at mature synapses. Mol. Cell. Neurosci 24, 442–450. [PubMed: 14572465]

Sigal YM, Zhou R, and Zhuang X. (2018). Visualizing and discovering cellular structures with super-resolution microscopy. Science 361, 880–887. [PubMed: 30166485]

Smith KR, and Kittler JT (2010). The cell biology of synaptic inhibition in health and disease. Curr. Opin. Neurobiol 20, 550–556. [PubMed: 20650630]

Smith KR, McAinsh K, Chen G, Arancibia-Carcamo IL, Haucke V, Yan Z, Moss SJ, and Kittler JT (2008). Regulation of inhibitory synaptic transmission by a conserved atypical interaction of GABA(A) receptor beta- and gamma-subunits with the clathrin AP2 adaptor. Neuropharmacology 55, 844–850. [PubMed: 18662706]

Smith KR, Muir J, Rao Y, Browarski M, Gruenig MC, Sheehan DF, Haucke V, and Kittler JT (2012). Stabilization of GABA(A) receptors at endocytic zones is mediated by an AP2 binding motif within the GABA(A) receptor β3 subunit. J. Neurosci 32, 2485–2498. [PubMed: 22396422]

Smith KR, Davenport EC, Wei J, Li X, Pathania M, Vaccaro V, Yan Z, and Kittler JT (2014). GIT1 and βPIX are essential for GABA(A) receptor synaptic stability and inhibitory neurotransmission. Cell Rep. 9, 298–310. [PubMed: 25284783]

Smith KR, Rajgor D, and Hanley JG (2017). Differential regulation of the Rac1 GTPase-activating protein (GAP) BCR during oxygen/glucose deprivation in hippocampal and cortical neurons. J. Biol. Chem 292, 20173–20183. [PubMed: 29046349]

Specht CG, Izeddin I, Rodriguez PC, El Beheiry M, Rostaing P, Darzacq X, Dahan M, and Triller A. (2013). Quantitative nanoscopy of inhibitory synapses: counting gephyrin molecules and receptor binding sites. Neuron 79, 308–321. [PubMed: 23889935]

Südhof TC (2012). The presynaptic active zone. Neuron 75, 11–25. [PubMed: 22794257]

Tretter V, Jacob TC, Mukherjee J, Fritschy JM, Pangalos MN, and Moss SJ (2008). The clustering of GABA(A) receptor subtypes at inhibitory synapses is facilitated via the direct binding of receptor alpha 2 subunits to gephyrin. J. Neurosci 28, 1356–1365. [PubMed: 18256255]

Tretter V, Kerschner B, Milenkovic I, Ramsden SL, Ramerstorfer J, Saiepour L, Maric HM, Moss SJ, Schindelin H, Harvey RJ, et al. (2011). Molecular basis of the γ-aminobutyric acid A receptor α3 subunit interaction with the clustering protein gephyrin. J. Biol. Chem 286, 37702–37711. [PubMed: 21880742]

Twelvetrees AE, Yuen EY, Arancibia-Carcamo IL, MacAskill AF, Rostaing P, Lumb MJ, Humbert S, Triller A, Saudou F, Yan Z, and Kittler JT (2010). Delivery of GABAARs to synapses is mediated by HAP1-KIF5 and disrupted by mutant huntingtin. Neuron 65, 53–65. [PubMed: 20152113]

Tyagarajan SK, and Fritschy JM (2014). Gephyrin: a master regulator of neuronal function? Nat. Rev. Neurosci 15, 141–156. [PubMed: 24552784]

Author Manuscript Author Manuscript Author Manuscript Author Manuscript

Tyagarajan SK, Ghosh H, Yévenes GE, Nikonenko I, Ebeling C, Schwerdel C, Sidler C, Zeilhofer HU, Gerrits B, Muller D, and Fritschy JM (2011). Regulation of GABAergic synapse formation and plasticity by GSK3β-dependent phosphorylation of gephyrin. Proc. Natl. Acad. Sci. USA 108, 379–384. [PubMed: 21173228]

Tyagarajan SK, Ghosh H, Yévenes GE, Imanishi SY, Zeilhofer HU, Gerrits B, and Fritschy J-M (2013). Extracellular signal-regulated kinase and glycogen synthase kinase 3β regulate gephyrin postsynaptic aggregation and GABAergic synaptic function in a calpain-dependent mechanism. J. Biol. Chem 288, 9634–9647. [PubMed: 23408424]

Wang J, Liu S, Haditsch U, Tu W, Cochrane K, Ahmadian G, Tran L, Paw J, Wang Y, Mansuy I, et al. (2003). Interaction of calcineurin and type-A GABA receptor gamma 2 subunits produces long-term depression at CA1 inhibitory synapses. J. Neurosci 23, 826–836. [PubMed: 12574411]

Yamasaki T, Hoyos-Ramirez E, Martenson JS, Morimoto-Tomita M, and Tomita S. (2017). GARLH family proteins stabilize $GABA_A$ receptors at synapses. Neuron 93, 1138–1152.e6. [PubMed: 28279354]

Yang X, Le Corronc H, Legendre P, Triller A, and Specht CG (2021). Differential regulation of glycinergic and GABAergic nanocolumns at mixed inhibitory synapses. EMBO Rep. 22, e52154.

Zhan R-Z, Nadler JV, and Schwartz-Bloom RD (2006). Depressed responses to applied and synaptically-released GABA in CA1 pyramidal cells, but not in CA1 interneurons, after transient forebrain ischemia. J. Cereb. Blood Flow Metab 26, 112–124. [PubMed: 15959457]

Author Manuscript Author Manuscript Author Manuscript Author Manuscript

Highlights

- Inhibitory synaptic components are sequentially lost during synapse disassembly
- Excitotoxicity induces rapid $GABA_AR$ nanoscale rearrangements and synaptic dispersal
- Loss of $GABA_ARs$ and gephyrin from synapses is regulated by independent mechanisms
- Calcineurin and calpain activation mediate excitotoxic GABAergic synapse disassembly

Author Manuscript Author Manuscript Author Manuscript Author Manuscript

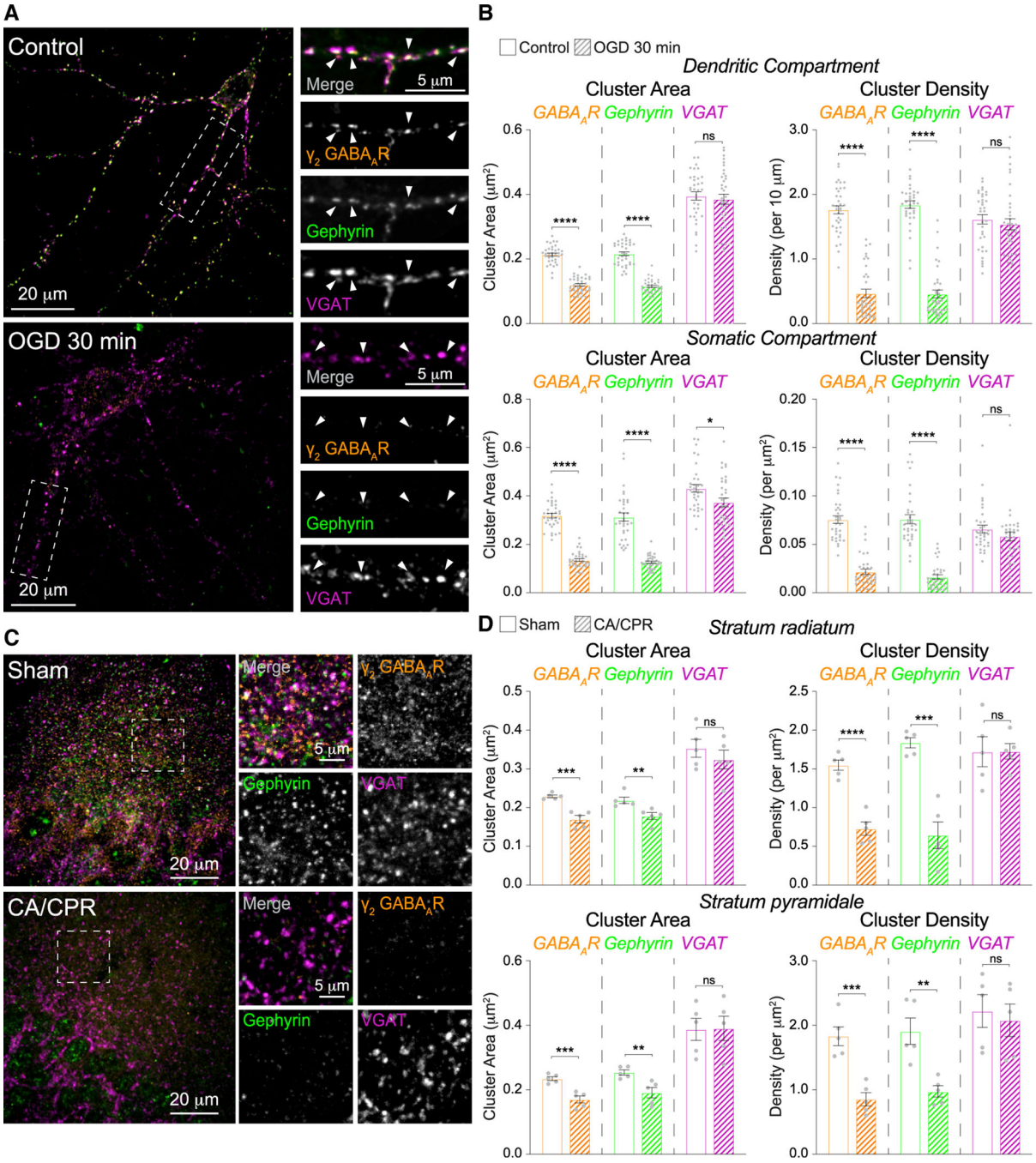

Figure 1. Ischemic insult induces rapid removal of synaptic GABA$_A$Rs and gephyrin from inhibitory synaptic sites

(A) Confocal images of hippocampal neurons labeled for synaptic and surface GABA$_A$R-γ2, gephyrin, and VGAT. Neurons were treated with control or OGD conditions for 30 min. Arrows, VGAT-positive synapses.

(B) Quantification of cluster area and density from (A) for dendritic and somatic compartments, n = 35–36 neurons per condition.

(C) Representative images of CA1 hippocampal slices from sham or CA/CPR mice labeled for GABA$_A$R-γ2, gephyrin, and VGAT.

Author Manuscript Author Manuscript Author Manuscript Author Manuscript

(D) Quantification of cluster area and density from (C) for *S. radiatum* and *pyramidale* regions; n = 5 mice per condition.

Values represent mean ± SEM. *p < 0.05; **p < 0.01; ***p < 0.001; ****p < 0.0001; Student's t test (B and D). See also Figure S1.

Author Manuscript Author Manuscript Author Manuscript Author Manuscript

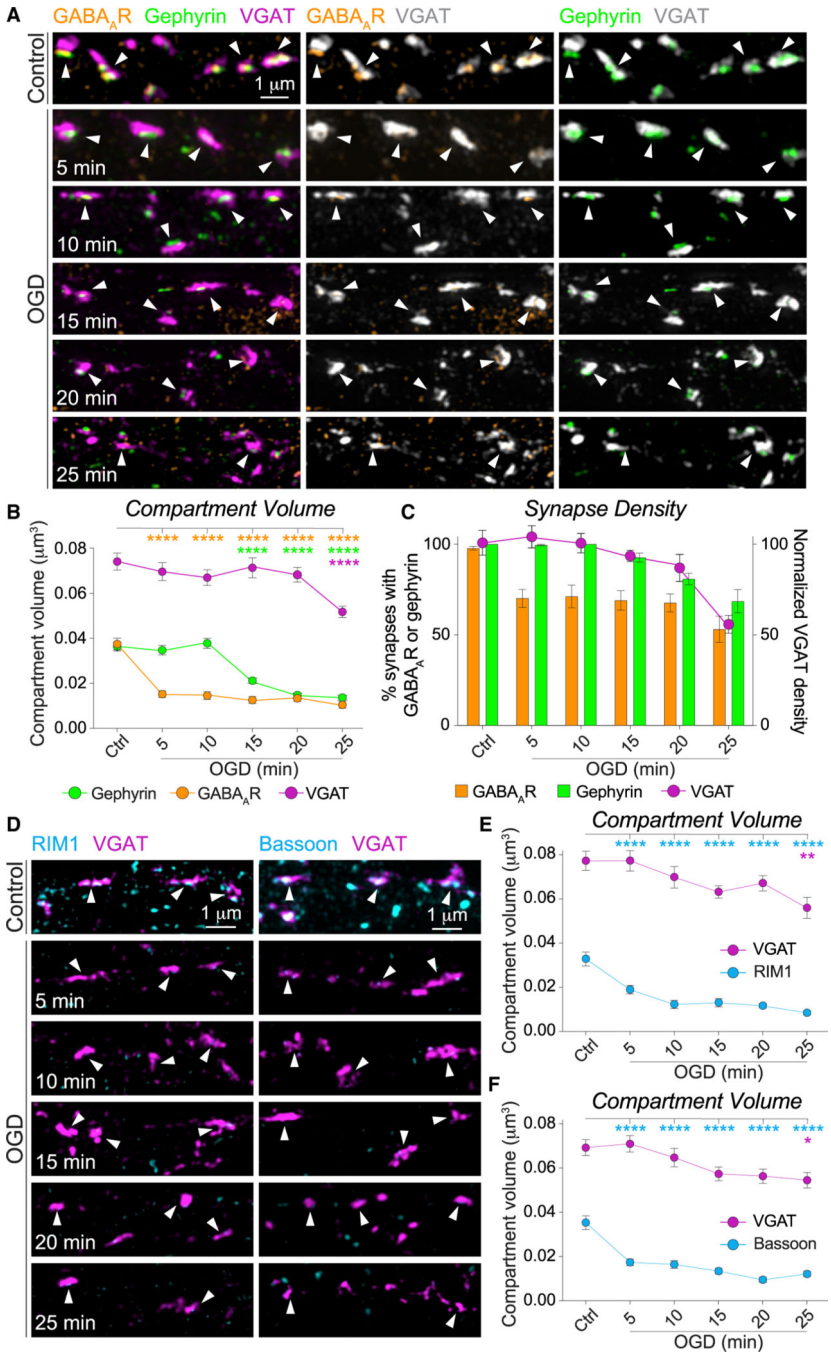

Figure 2. GABA$_A$Rs and presynaptic active zone proteins are lost prior to gephyrin during excitotoxic-induced inhibitory synapse disassembly

(A) 3D-SIM maximum projections of hippocampal neuronal dendrites labeled for surface GABA$_A$Rs, gephyrin, and VGAT. Arrows, VGAT-positive synapses. Neurons were fixed at 5-min intervals up to 25 min of OGD.

(B) Quantification of GABA$_A$R, gephyrin, and VGAT compartment volumes at 5-min intervals throughout the 25-min OGD insult. n = 158–166 synapses. Colored stars compare statistical significance to the control condition.

Author Manuscript Author Manuscript Author Manuscript Author Manuscript

(C) Quantification of percentage of synapses (VGAT +ve) with $GABA_A$Rs or gephyrin present at each time point (bars). VGAT density is plotted as a percentage normalized to the control (line). n = 158–166 synapses.

(D) 3D-SIM maximum projections of hippocampal neuronal dendrites labeled for VGAT and the active zone proteins RIM1 (left) or Bassoon (right). Arrows, VGAT-positive synapses.

(E and F) Quantification of VGAT compartment volumes with either (E) RIM1 or (F) Bassoon compartment volumes at 5-min intervals throughout the 25-min OGD insult. n = 115–122 synapses. Colored stars compare statistical significance to the control condition. Values represent mean or percentage of neuron population ± SEM. *p < 0.05; **p < 0.01; ****p < 0.0001; one-way ANOVA; Bonferroni post hoc test (B, E, and F).

See also Figure S2.

Author Manuscript Author Manuscript Author Manuscript Author Manuscript

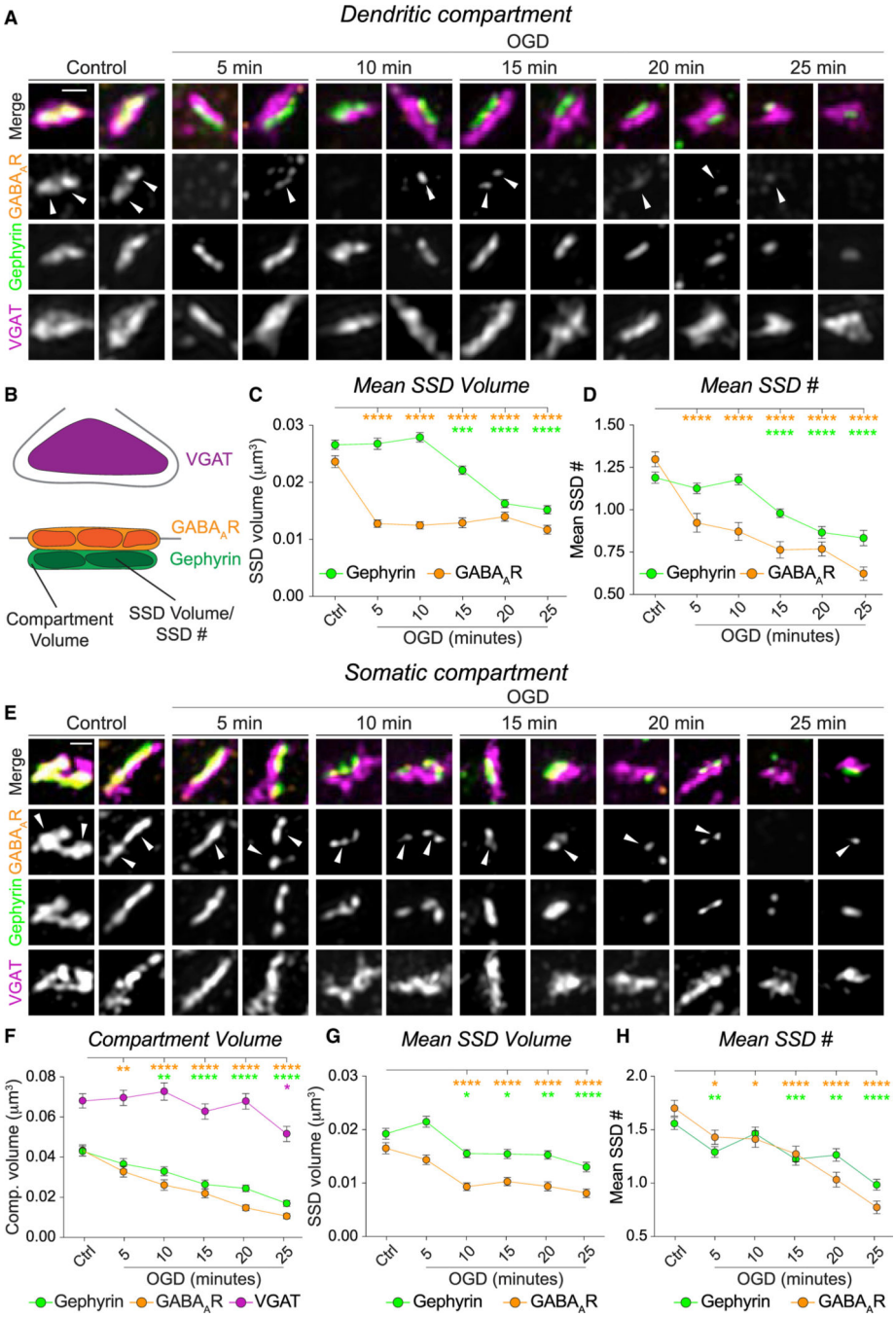

Figure 3. Rapid nanoscale alterations to GABA$_A$R sub-synaptic domains (SSDs) immediately following OGD induction

(A) 3D-SIM maximum projections of individual dendritic inhibitory synapses labeled for synaptic and surface GABA$_A$Rs, gephyrin, and VGAT. Neurons were fixed at 5-min intervals up to a maximum 25 min of OGD. Arrows, individual GABA$_A$R SSDs. Scale bar represents 500 nm.

(B) Schematic of SSD parameters measured by 3D-SIM segmentation.

Author Manuscript Author Manuscript Author Manuscript Author Manuscript

(C and D) Quantification of the (C) mean SSD volume and (D) mean number of SSDs per compartment. n = 158–166 synapses; stars compare statistical significance to the control condition.

(E) 3D-SIM maximum projections of individual somatic inhibitory synapses labeled for synaptic and surface $GABA_A$Rs, gephyrin, and VGAT. Neurons were fixed at 5-min intervals up to a maximum 25 min of OGD. Arrows, individual $GABA_A$R SSDs. Scale bar represents 500 nm.

(F–H) Quantification of the (F) compartment volume, (G) mean SSD volume, and (H) mean number of SSDs per compartment. n = 115–122 synapses; stars compare statistical significance to the control condition.

Values represent mean ± SEM. *$p < 0.05$, **$p < 0.01$, ***$p < 0.001$, and ****$p < 0.0001$; one-way ANOVA; Bonferroni post hoc test (C, D, and F–H). See also Figure S3.

Author Manuscript Author Manuscript Author Manuscript Author Manuscript

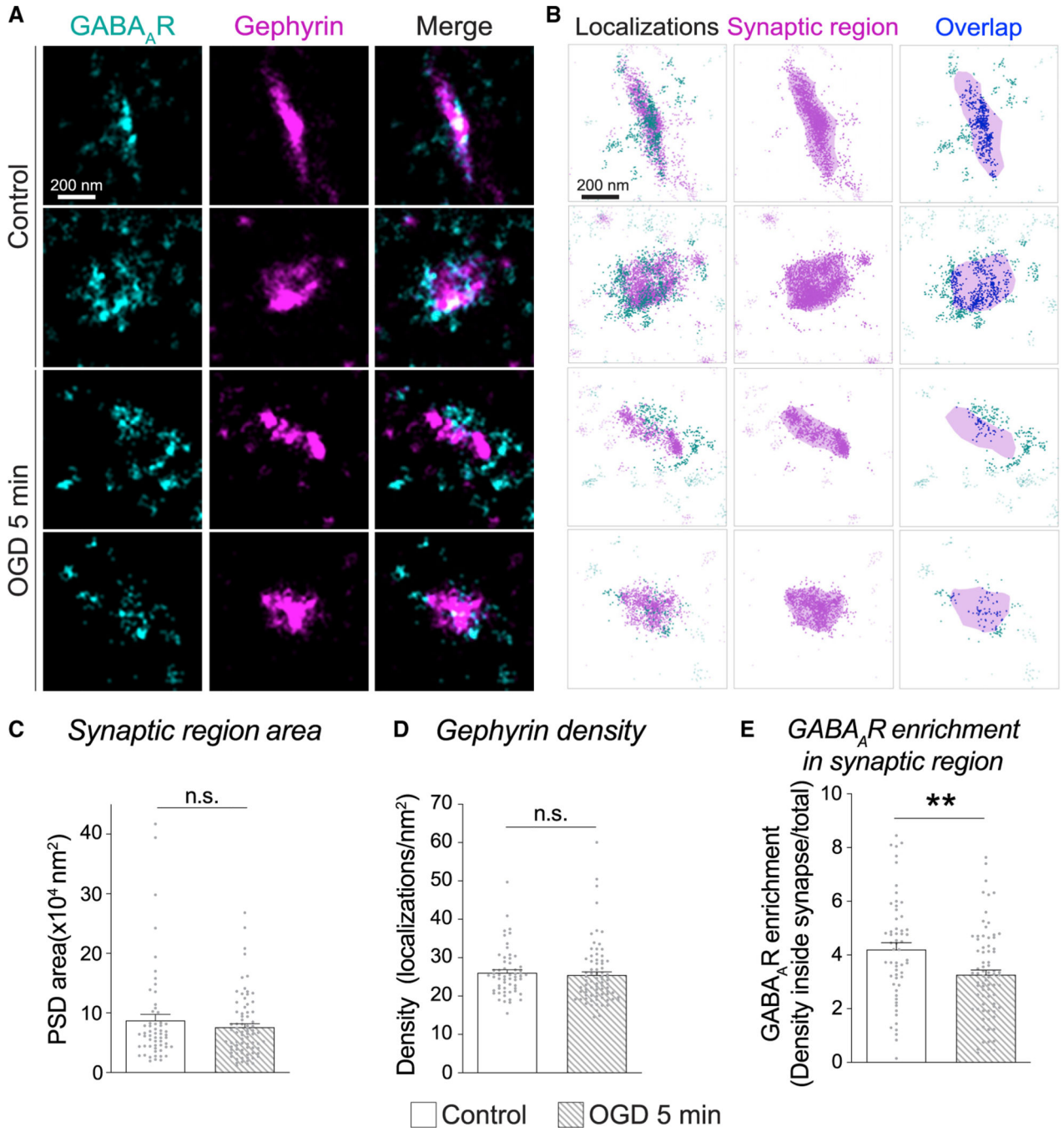

Figure 4. OGD induces rapid GABA$_A$R dispersal from inhibitory postsynaptic sites

(A) dSTORM images of VGAT-positive inhibitory synapses under control conditions or following a 5-min OGD insult. Surface GABA$_A$Rs (γ2; teal) and gephyrin (magenta) are shown.

(B) Localization maps of images in (A) showing individual localization points of GABA$_A$Rs (teal) and gephyrin (magenta). The shaded magenta region delineates the gephyrin scaffold boundary. GABA$_A$R localizations that overlap with the gephyrin scaffold are represented in dark blue.

Author Manuscript Author Manuscript Author Manuscript Author Manuscript

(C–E) Quantification of the (C) gephyrin scaffold boundary area, (D) mean gephyrin localization density, and (E) $GABA_AR$ localization enrichment within the synaptic region in control and OGD conditions; n = 58–78 synapses per condition.
Values represent mean ± SEM. **p < 0.01; Mann-Whitney tests (C–E).

Author Manuscript Author Manuscript Author Manuscript Author Manuscript

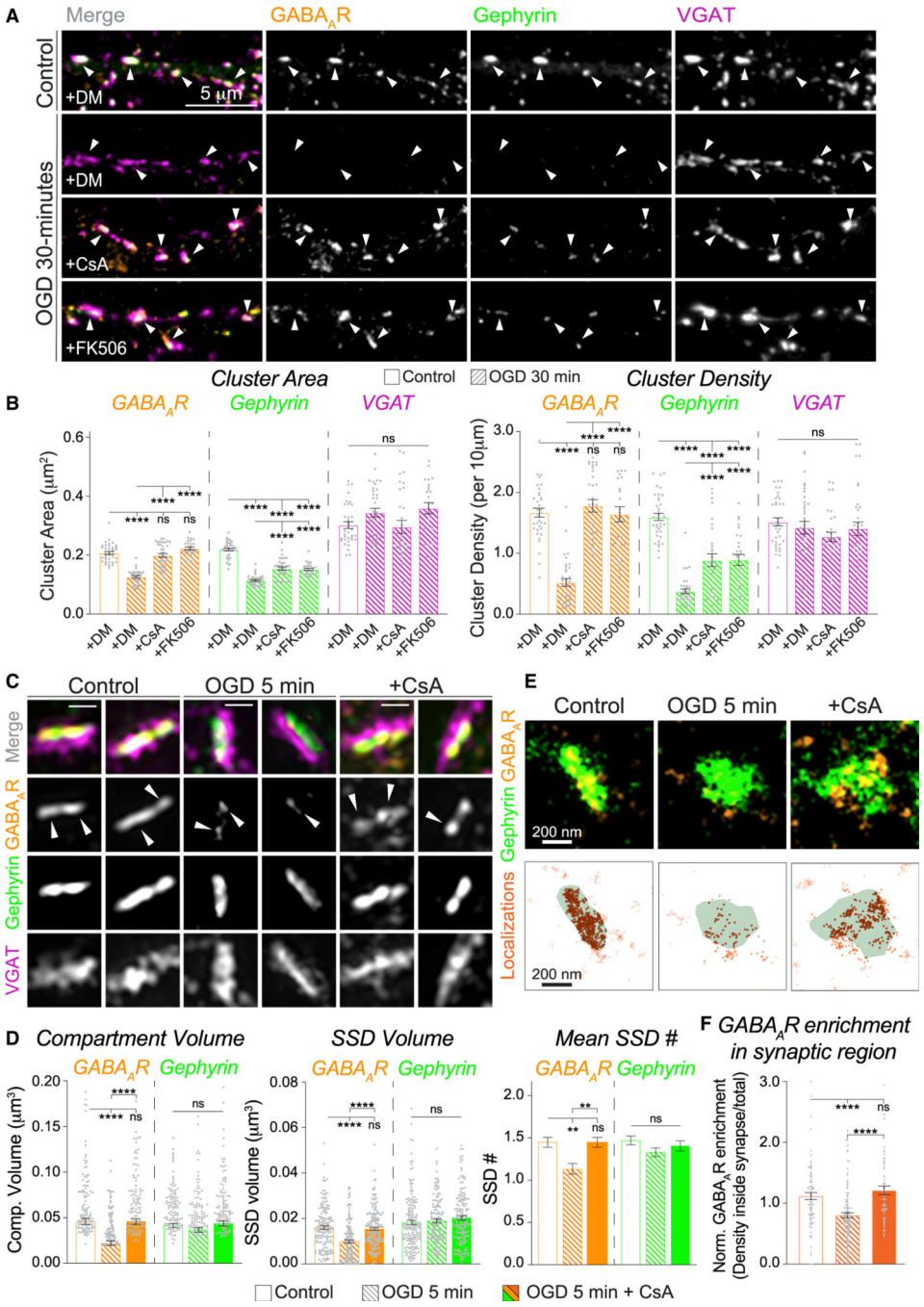

Figure 5. Calcineurin activity is required for OGD-induced GABA$_A$R nanoscale reorganization and removal from synapses

(A) Confocal images of dendritic segments from hippocampal neurons labeled for synaptic GABA$_A$Rs, gephyrin, and VGAT. Neurons were treated with control or OGD conditions for 30 min in the presence of DMSO (DM), cyclosporin A (CsA) (5 µM), or FK506 (5 µM). Arrows, VGAT-positive synapses.

(B) Quantification of synapse cluster area and density from images in (A); n = 27–33 neurons.

Author Manuscript Author Manuscript Author Manuscript Author Manuscript

(C) 3D-SIM maximum projections of individual synapses labeled for synaptic $GABA_A$Rs, gephyrin, and VGAT. Neurons were treated with control or OGD conditions for 5 min in the presence of DM or CsA. Arrows, individual $GABA_A$R SSDs. Scale bars represent 500 nm.
(D) Quantification of compartment volume, mean SSD volume, and mean SSD number per compartment for gephyrin and $GABA_A$Rs. n = 159–163 synapses.
(E) dSTORM images of VGAT-positive inhibitory synapses labeled for surface $GABA_A$Rs (orange) and gephyrin (green). Neurons were treated with control or OGD conditions for 5 min in the presence of DM or CsA. Localization maps of dSTORM images show localization points for $GABA_A$Rs and gephyrin. The shaded green region delineates the gephyrin scaffold boundary. $GABA_A$R localizations that overlap with gephyrin are represented in dark orange.
(F) Quantification of the $GABA_A$R localization enrichment in the synaptic region following control, OGD 5 min, and OGD 5 min + CsA treatments; n = 65–84 synapses per condition. Values represent mean ± SEM. **$p < 0.01$ and ****$p < 0.0001$; one-way ANOVA; Bonferroni post hoc test (B, D, and F). See also Figure S4.

Author Manuscript Author Manuscript Author Manuscript Author Manuscript

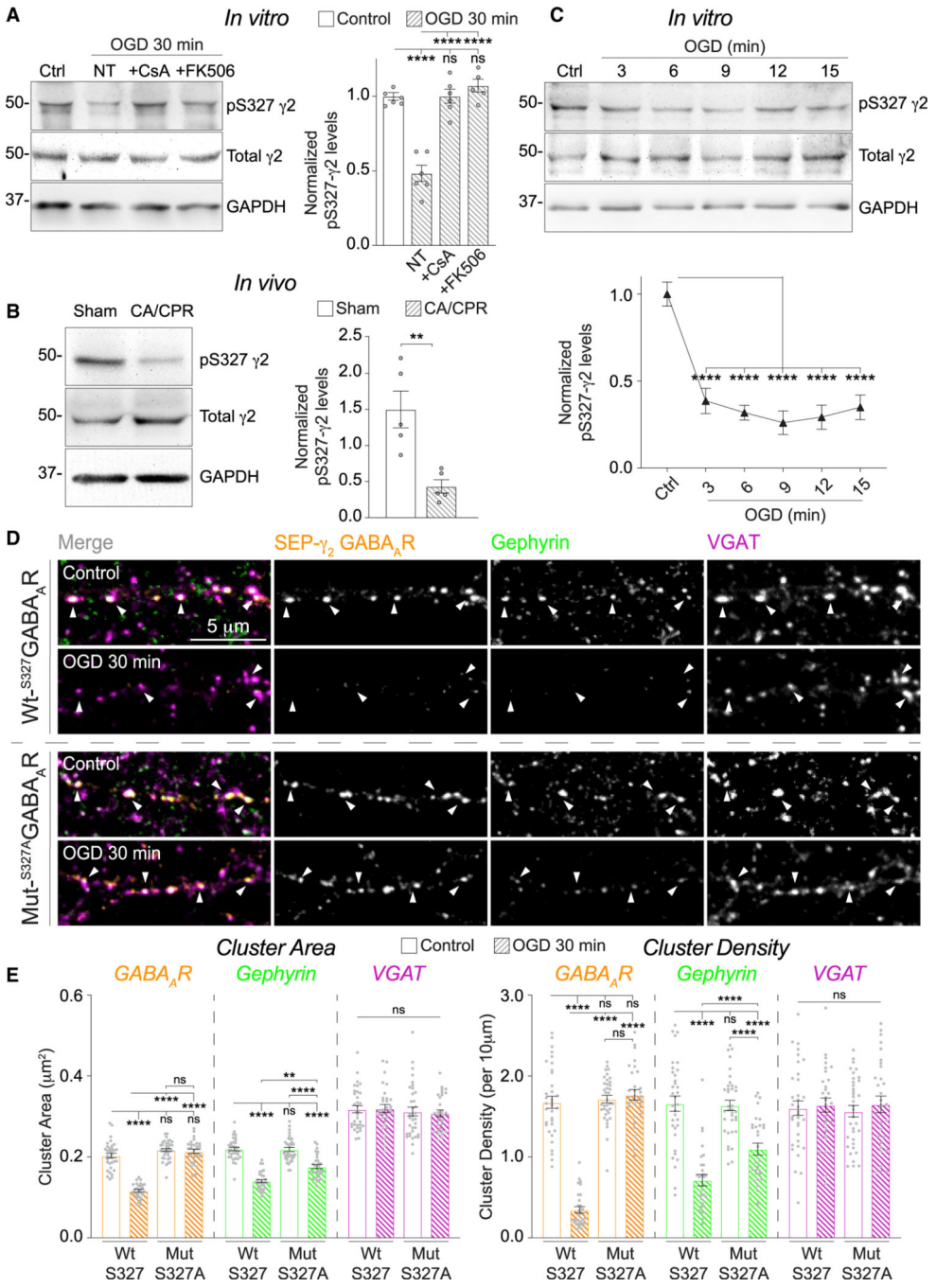

Figure 6. GABA$_A$R-γ2 serine 327 regulates OGD-dependent GABA$_A$R declustering

(A) Hippocampal neuronal lysates analyzed following a 30-min OGD insult with and without CaN inhibitors; CsA (5 μM) and FK506 (5 μM). Phospho-GABA$_A$R-γ2 was normalized to total GABA$_A$R-γ2. n = 5–6.

(B)Hippocampal crude membrane lysates from mice following sham or CA/CPR procedure. Phospho-GABA$_A$R-γ2 was normalized to total GABA$_A$R-γ2. n = 5 animals per condition.

(C) Hippocampal neuronal lysates analyzed at 3-min intervals up to a maximum of a 15-min OGD insult. Phospho-GABA$_A$R-γ2 was normalized to total GABA$_A$R-γ2. n = 5.

Author Manuscript Author Manuscript Author Manuscript Author Manuscript

(D) Confocal images of dendritic segments from hippocampal neurons expressing super-ecliptic pHluorin (SEP)-tagged $GABA_AR$-γ2 and labeled for gephyrin and VGAT. Neurons expressing WT or Mut γ2-S327 were treated with control or OGD conditions for 30 min. Arrows, VGAT-positive synapses.

(E) Quantification of synapse cluster area and density from (D); n = 30–36 neurons. Values represent mean ± SEM. **p < 0.01 and ****p < 0.0001; one-way ANOVA; Bonferroni post hoc test (A, C, and E) or t test (B). See also Figure S5.

Author Manuscript Author Manuscript Author Manuscript Author Manuscript

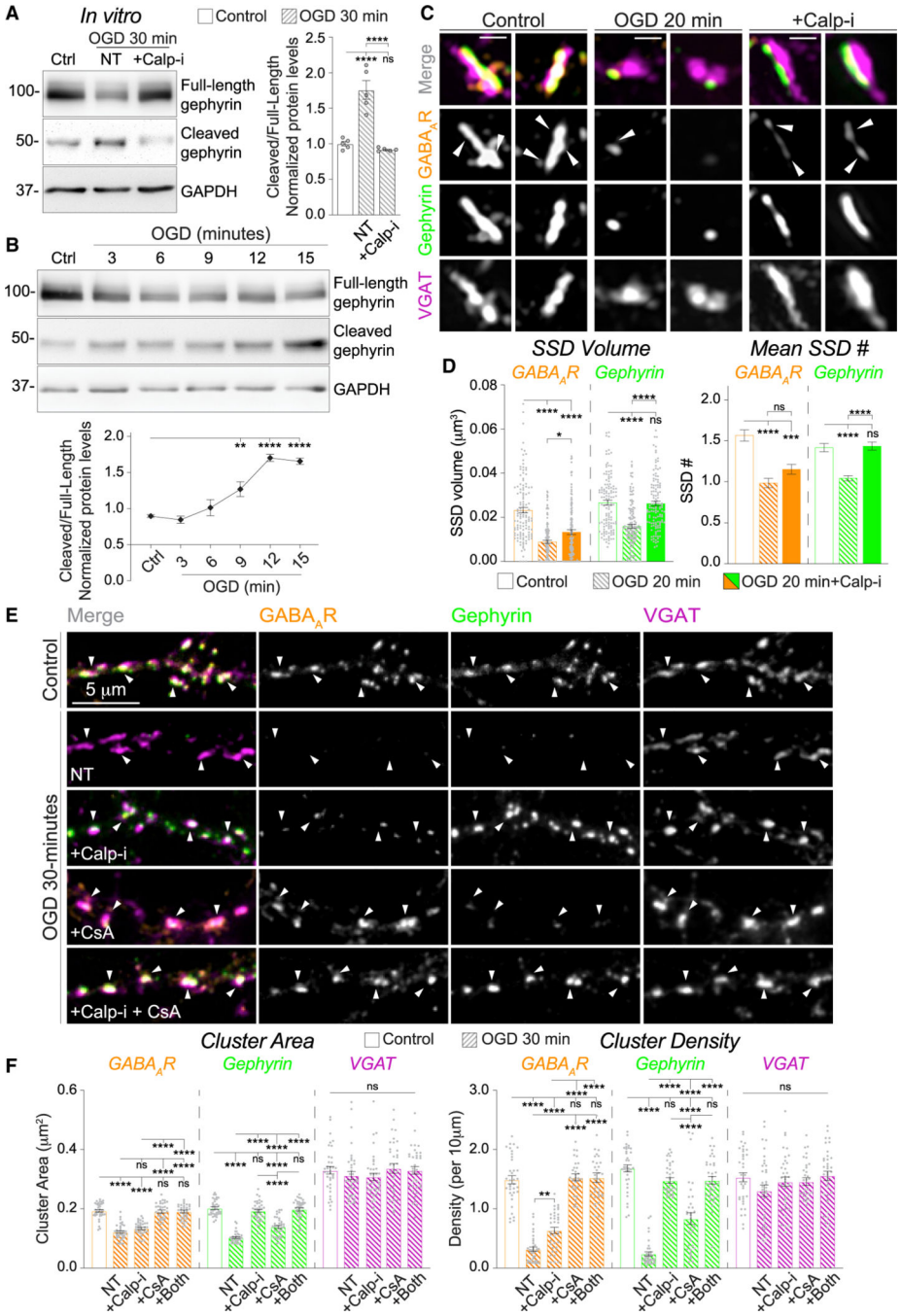

Figure 7. Calcineurin and calpain inhibition are both required to preserve inhibitory synaptic structure following OGD

(A) Hippocampal neuronal lysates analyzed following a 30-min OGD insult in the absence and presence of a calpain inhibitor (MDL-28170, Calp-i 100 µM). Cleaved gephyrin levels (50 kDa) were normalized to full-length gephyrin levels (~100 kDa); n = 5.

(B) Hippocampal neuronal lysates analyzed at 3-min intervals up to 15 min of OGD. Cleaved gephyrin levels were normalized to full-length gephyrin levels; n = 5.

(C) 3D-SIM maximum projections of inhibitory synapses labeled for surface GABA$_A$Rs, gephyrin, and VGAT. Neurons were treated with control or OGD conditions for 20 min

Author Manuscript Author Manuscript Author Manuscript Author Manuscript

in the presence of DMSO (DM) or Calp-i. Arrows, individual $GABA_AR$ SSDs. Scale bars represent 500 nm.

(D) Quantification of the mean SSD volume and number per compartment for gephyrin and $GABA_ARs$. n = 130–133 synapses.

(E) Confocal images of dendrites from hippocampal neurons labeled for surface $GABA_ARs$, gephyrin, and VGAT. Neurons were treated with control or OGD conditions for 30 min in the presence of CsA, Calp-i, or both. Arrows, VGAT-positive synapses.

(F) Quantification of cluster area and density from images in (E); n = 35–36 neurons per condition.

Values represent mean ± SEM. *p < 0.05, **p < 0.01, and ****p < 0.0001; one-way ANOVA; Bonferroni post hoc test (A, B, D, and F). See also Figure S6.

Author Manuscript Author Manuscript Author Manuscript Author Manuscript

KEY RESOURCES TABLE

Reagent or resource	Source	Identifier
Antibodies		
$GABA_AR$-γ2 (imaging)	Synaptic Systems	Cat. #224 004; AB_10594245
$GABA_AR$-α1 (imaging)	Synaptic Systems	Cat. #224 203; AB_2232180
Anti-GFP (imaging)	ThermoFisher	Cat. #11122; AB_221569
Gephyrin (mAB7a; imaging)	Synaptic Systems	Cat. #147 011; AB_887717
Gephyrin (3B11; imaging)	Synaptic Systems	Cat. #147 111; AB_2619837
VGAT (rabbit; imaging)	Synaptic Systems	Cat. #131 003; AB_887869
VGAT (guinea pig; imaging)	Synaptic Systems	Cat. #131 004; AB_887873
RIM1 (imaging)	Synaptic Systems	Cat. #140 003; AB_887774
Bassoon (imaging)	Synaptic Systems	Cat. #141 004; AB_2290619
Neuroligin 2 (NL2; imaging)	Synaptic Systems	Cat. #129 511; AB_2619813
GAD1/67 (imaging)	Synaptic Systems	Cat. #198 003; AB_2107720
$GABA_AR$-β3 (imaging)	NeuroMab	Cat. #75-149; AB_10673389
Anti-guinea pig Alexa Fluor - 568	Life Technologies	Cat. #11075; AB_141954
Anti-guinea pig Alexa Fluor - 647	Abcam	Cat. #150187; AB_2827756
Anti-mouse Alexa Fluor - 488	Life Technologies	Cat. #21202; AB_141607
Anti-rabbit Alexa Fluor - 488	Life Technologies	Cat. #21206; AB_2535792
Anti-rabbit Alexa Fluor - 647	Life Technologies	Cat. #31573; AB_2536183
CF568	Biotum	Cat. #20100-1; AB_10853601
$GABA_AR$-γ2 (WB)	NeuroMab	Cat. #75-442; AB_2566822
$GABA_AR$-α1 (WB)	NeuroMab	Cat. #75-136; AB_10697873
$GABA_AR$-β3 (imaging & WB)	NeuroMab	Cat. #75-149; AB_10673389
$GABA_AR$-γ2-pS327 (WB)	Abcam	Cat. #612-401-D52; AB_1268933
Gephyrin (WB)	Synaptic Systems	Cat. #147 111; AB_2619837
GAPDH	GeneTex	Cat. #GTX627408; AB_11174761
HRP-conjugated goat anti-mouse	BioRad	Cat. #170-6516; AB_11125547
HRP-conjugated goat anti-rabbit	BioRad	Cat. #170-6515; AB_11125142
Chemicals, peptides, and recombinant proteins		
Cyclosporin A (CsA)	Tocris Bioscience	Cat. #1101
FK506	Tocris Bioscience	Cat. #3631
MDL-28170 (Calp-i)	Tocris Bioscience	Cat. #1146
Pierce Sulfo-NHS-LC-Biotin	ThermoFisher	Cat. #PG82075
Pierce NeutrAvidin	ThermoFisher	Cat. #29201
Lipofectamine 2000	ThermoFisher	Cat. #11668027
Critical commercial assays		
PLA mouse/rabbit kit	Sigma	Cat. #DUO92101

Author Manuscript Author Manuscript Author Manuscript Author Manuscript

Reagent or resource	Source	Identifier
Experimental models: organisms/strains		
Rat, Sprague Dawley Charles River	Charles River	RRID: RGD_734476
Mice, C57BL/6	Jackson Laboratory	N/A
Oligonucleotides		
Primer: S327A mutant Forward: F-5′ ccggaagccagccaaggataaag 3′	This paper	N/A
Primer: S327A mutant Reverse: R-3′ ggccttcggtcggttcctatttc 5′	This Paper	N/A
Recombinant DNA		
SEP-GABA$_A$R-γ2	Addgene	Muir et. al, 2010
Software and algorithms		
Prism 9	GraphPad	https://www.graphpad.com/scientific-software/prism/
ImageJ	NIH	https://imagej.nih.gov/ij/
NIS Elements	Nikon	https://www.microscope.healthcare.nikon.com/products/software
Mosaic Suite (FIJI/ImageJ plugin)	Mosaic Group	https://sbalzarini-lab.org/
MATLAB	Mathworks	https://www.mathworks.com